

Universal Transient Stability Analysis: A Large Language Model-Enabled Power System Dynamics Prediction Framework

Chao Shen^a, Ke Zuo^a, Mingyang Sun^{b,*}

^a*College of Control Science and Engineering, Zhejiang University, 310027, Hangzhou, China*

^b*School of Advanced Manufacturing and Robotics, Peking University, 100871, Beijing, China*

Abstract

Existing dynamics prediction frameworks for transient stability analysis (TSA) fail to achieve multi-scenario "universality"—the inherent ability of a single, pre-trained architecture to generalize across diverse operating conditions, unseen faults, and heterogeneous systems. To address this, this paper proposes TSA-LLM, a large language model (LLM)-based universal framework that models multivariate transient dynamics prediction as a univariate generative task with three key innovations: First, a novel data processing pipeline featuring channel independence decomposition to resolve dimensional heterogeneity, sample-wise normalization to eliminate separate stable/unstable pipelines, and temporal patching for efficient long-sequence modeling; Second, a parameter-efficient freeze-and-finetune strategy that augments the LLM's architecture with dedicated input embedding and output projection layers while freezing core transformer blocks to preserve generic feature extraction capabilities; Third, a two-stage fine-tuning scheme that combines teacher forcing, which feeds the model ground-truth data during initial training, with scheduled sampling, which gradually shifts to leveraging model-generated predictions, to mitigate cumulative errors in long-horizon iterative prediction. Comprehensive testing demonstrates the framework's universality, as TSA-LLM trained solely on the New England 39-bus system achieves zero-shot generalization to mixed stability conditions and unseen

*Corresponding Author

faults, and matches expert performance on the Iceland 189-bus system with only 5% fine-tuning data. Additional cross-system experiments on the IEEE 68-bus and IEEE 118-bus systems, together with stability metrics and PEBS comparison, further confirm TSA-LLM’s strong zero-shot transferability and data-efficient adaptation. This multi-scenario versatility validates a universal framework that eliminates scenario-specific retraining and achieves scalability via large-scale parameters and cross-scenario training data.

Keywords: Deep learning, data-driven methods, transient stability analysis, dynamic trajectory prediction, pre-trained large language model, iterative prediction.

1. Introduction

The increasing penetration of renewable energy sources reduces system inertia and elevates operational uncertainty, posing significant challenges to grid stability [1, 2]. Consequently, modern power systems are increasingly susceptible to contingencies, demanding more robust analytical frameworks. Power system stability is the ability of an electric power system, for a given initial operating condition, to regain a state of operating equilibrium after being subjected to a physical disturbance, with most system variables bounded so that practically the entire system remains intact [3]. A key aspect of this broad stability notion is transient stability analysis (TSA), which assesses whether the system can maintain synchronism and reach an acceptable post-disturbance equilibrium following a large disturbance (e.g., short-circuit faults, line/generator tripping), as manifested in the post-disturbance transient dynamics [4, 5, 3]. Accordingly, the core objective of this work is to support TSA by rapidly predicting post-fault trajectories of key state variables (e.g., rotor angle and speed) from limited PMU observations, thereby enabling timely stability assessment and emergency decision-making.

TSA is critical for preventive control and emergency response, enabling grid operators to enhance resilience against cascading failures and ensure reliable operation under evolving operating conditions (OCs) [6]. Conventionally, the dynamic behavior of power systems is typically described by nonlinear differential-algebraic equations (DAEs), which are numerically solved via time-domain simulation (TDS) methods [7]. While TDS provides high-fidelity temporal resolution, its computational intensity and scalability challenges limit its online practicality [8]. Alternatively, direct methods evaluate transient

stability without performing long-horizon time-domain simulation. Following the taxonomy summarized in [9], mainstream direct methods can be categorized into three groups. (i) EAC-based equivalencing methods (e.g., the Extended Equal Area Criterion (EEAC) [10]) extend the equal-area criterion from SMIB to multi-machine systems by coherent-grouping and two-machine equivalencing [11]. In practice, they often become hybrid integral-direct methods due to the need for trajectory-dependent grouping or auxiliary integration. (ii) Global energy-function (topological) methods [12] construct a global energy function $V(x)$ and characterize the stability region via the closest controlling unstable equilibrium point (UEP) [13]. A representative practical variant is the Potential Energy Boundary Surface (PEBS) method, which approximates the stability boundary by locating the first local maximum of the potential energy along the fault-on trajectory, thereby avoiding explicit UEP computation [14]. While these methods provide clear geometric interpretation and stability margins, they rely on strong model assumptions (existence of a global energy function) and typically still require obtaining the fault-clearing state. (iii) Local Lyapunov-function (LLF) methods [9, 15, 16] construct a Lyapunov function locally around the post-fault stable equilibrium and certify stability via an invariant sublevel set, which can, in principle, avoid numerical integration and UEP computation. However, traditional LLF conditions and set/derivative bounds may introduce conservatism. Despite their theoretical elegance, direct methods face challenges in model generality, numerical tractability, and conservatism in large-scale online settings [9, 17].

The widespread deployment of phasor measurement units (PMUs) has spurred the development of data-driven TSA. These methods learn the mapping between system measurements and stability-related features, enabling rapid online applications such as real-time stability classification [18, 19, 20, 21, 22, 17, 23] and stability margin estimation [24, 25, 26]. Early research in this domain was dominated by classical machine learning. For instance, artificial neural networks were applied to perform rapid transient stability classification [18], while support vector machines demonstrated robust post-fault stability prediction using synchrophasor data [27, 19]. Concurrently, decision trees were used to extract critical stability indicators through offline feature ranking, facilitating periodic updates to security rules [28, 20]. More recent research has shifted toward deep learning (DL) frameworks to improve both prediction accuracy and model interpretability. To enhance explainability, a time-adaptive attention-based gated recurrent unit (GRU) was developed to visualize feature importance [21], while other work inte-

grated decision tree path length constraints into the DL loss function [22]. For performance improvement, hybrid architectures combining convolutional neural networks (CNNs) and long short-term memory (LSTMs) were proposed for stability classification and oscillation prediction [17, 4]. Beyond binary classification, significant effort has focused on directly predicting stability margins, often derived from the critical clearing time (CCT). Notable methods include an ensemble DL framework with dynamic error correction for CCT estimation [24] and a two-level CNN regression model that predicts margins from 2-D images of system trajectories [25].

Although existing data-driven models provide rapid and accurate stability classification, this binary output offers limited actionable insight for system operators [8, 5]. Consequently, TSA research has shifted toward predicting detailed dynamic trajectories, which are critical for informing corrective actions such as load shedding or out-of-step (OOS) SG tripping [5]. One prominent approach involves physics-informed neural networks (PINNs), which incorporate physical constraints as regularization terms to predict system dynamics [29]. However, the applicability of early PINN models was often limited to stable OCs. Subsequent work on physics-following neural networks (PFNNs) has sought to improve generalization across both stable and unstable cases by introducing time-varying algebraic parameters and supervised initialization into the PINN framework [1]. Other notable strategies include using LSTMs with separate processing pipeline for stable and unstable samples [5] and leveraging Fourier neural operators (FNOs) to predict transients in the frequency domain, thereby simplifying the learning task [30].

While the methods in [1, 5, 30] improve prediction accuracy in mixed stable/unstable OCs, they exhibit poor generalization to unseen faults. To address this, the stochastic variational deep kernel regressor (SVDKR)-based framework in [31] integrates an OOS detector for classifying SGs as stable or unstable. Dedicated SVDKR predictors are trained per stability class, followed by per-SG error correctors to refine unit-level predictions. Although this improves robustness, the parameter complexity and computational overhead hinder its scalability to large systems with numerous SGs. The deep neural representation (DNR) framework was proposed to mitigate these issues [8], using a unified graph attention and GRU architecture to predict dynamics in a single model. This design enhances performance under unseen faults but suffers from significant cumulative error amplification over long prediction horizons. More importantly, both the SVDKR [31] and DNR [8]

frameworks are designed for a single system. They lack the ability to generalize across heterogeneous power systems with different topologies and SG configurations, necessitating laborious retraining for each new system. This fundamental limitation—the absence of cross-system generalization capability—represents a critical knowledge gap in current TSA research, preventing the development of universal frameworks that could enable efficient knowledge transfer across diverse power networks.

As demonstrated in Table 2, existing frameworks suffer from pronounced performance degradation across diverse OCs, faults and system configurations. This systematic failure across multiple dimensions reveals a fundamental knowledge gap: *no existing TSA framework has achieved true universality*. This shortcoming motivates the pursuit of *universality* in TSA models, defined as a novel paradigm representing the intrinsic capability of a single pre-trained architecture to generalize robustly across mixed stable/unstable OCs, unseen fault events, and heterogeneous power systems. Universality enables a paradigm shift in TSA, analogous to the versatility of large language models (LLMs) in natural language processing, where a unified model adeptly addresses diverse dynamic trajectory prediction tasks [32]. By eliminating the need for scenario-specific retraining, a universal TSA framework provides foundational capabilities, most prominently exemplified by cross-system generalization. This feature enables efficient knowledge transfer from source-domain systems to large-scale target grids via few-shot adaptation, thereby minimizing computational simulation and labor costs associated with custom model development for diverse power networks [33]. Furthermore, universality inherently supports scalability, with performance systematically improving as model parameters and multi-scenario training datasets expand, which ensures adaptability to evolving grid complexities [34].

To avoid ambiguity, this paper adopts an operational definition of TSA “universality” along three explicit generalization axes: (i) *operating-condition universality*, i.e., robustness to mixed stable/unstable post-fault trajectories under diverse pre-fault operating points; (ii) *fault universality*, i.e., generalization to unseen fault locations/clearing conditions beyond those observed in training; and (iii) *cross-system universality*, i.e., reusing the *same* pre-trained architecture and model interface across heterogeneous networks with different SG configurations, with at most lightweight few-shot adaptation instead of full retraining.

However, achieving this universality requires overcoming three fundamental limitations: 1) Data processing rigidity, where current methods are

constrained to fixed input dimensionalities based on specific state variables, limiting scalability and requiring complete retraining for system changes or monitoblack SGs modifications [8], while frequently necessitating separate processing pipelines for stable/unstable dynamics that introduce computational overhead and misclassification risks [31, 5]; More importantly for cross-system generalization, the number of monitoblack SGs typically differs across networks, which directly changes the dimension of system-level stacked trajectories. This creates an inherent input/output dimension mismatch for pblackictors with fixed multivariate interfaces, and is a key reason why many existing models must be blackefined or retrained when transferring to a new system. 2) Architectural constraints, as prevalent recurrent neural network architectures (LSTMs [5] and GRUs [8]) suffer from vanishing gradient problems that impede long-range dependency modeling and inherently sequential processing that precludes parallel computation, creating critical bottlenecks for model scalability [35, 34]; 3) Training and error propagation, where the temporal asymmetry between short observation windows and extended pblackiction horizons in online TSA, combined with existing training schemes that lack explicit error suppression mechanisms, causes pblackiction errors to accumulate at each time step during iterative pblackiction, severely degrading long-term reliability [1, 36].

To address these challenges, this study proposes a pre-trained LLM-based universal dynamics pblackiction framework, TSA-LLM, that fundamentally reformulates multivariate transient dynamics pblackiction as a univariate generative sequence pblackiction task by leveraging pre-trained LLM parameters whose modality-agnostic sequence feature extraction and temporal dependency modeling capabilities transfer effectively to power-system dynamics (see Appendix A for empirical validation). The main contributions are:

1. To the best of the authors' knowledge, this is the first work to demonstrate universality in TSA through an LLM-based approach, achieving generalization across diverse OCs, unseen faults, and heterogeneous systems by systematically addressing fundamental limitations in data processing, model architecture, and fine-tuning schemes. This work establishes a new research direction by bridging generative sequence modeling and power system dynamics pblackiction. The challenge-to-design mapping is summarized in Table 1.
2. A novel data processing pipeline is designed and operates sequentially: channel-independence decouples multivariate dynamic sequences into

univariate streams, resolving dimensional heterogeneity across different systems and enabling system-agnostic processing; sample-wise normalization standardizes sequence samples via internal statistics, eliminating separate pipelines for stable/unstable OCs; temporal patching tokenizes sequences into semantic patches, enabling efficient long-sequence modeling while capturing high-level temporal patterns. This pipeline design transforms the problem from multivariate regression to univariate sequence generation, enabling direct compatibility with pre-trained LLM architectures.

3. A Generative Pre-trained Transformer (GPT) architecture is devised that incorporates dedicated input embedding and output projection alongside causal attention mechanisms for temporal dependency modeling. This represents the first application of pre-trained transformer architectures to power system dynamics prediction, leveraging transfer learning from large-scale sequence modeling tasks. The freeze-and-finetune strategy preserves pre-trained sequence feature extraction capability by freezing core transformer blocks (T-blocks) while selectively fine-tuning TSA-specific layers, achieving balance between knowledge retention and task adaptation.
4. A two-stage fine-tuning scheme is proposed to mitigate error propagation during iterative and generative dynamics prediction. This training strategy is specifically designed for autoregressive sequence generation in TSA, addressing the unique challenge of error accumulation in long-horizon prediction tasks. The initial teacher forcing (TeaF) stage ensures stable convergence by exclusively feeding ground-truth sequences as input. Subsequently, the scheduled sampling (SchS) stage enhances robustness by increasingly replacing ground-truth inputs with the model's own predictions, thereby compelling the model to correct for self-generated errors.

Table 1: Challenge-to-design mapping

Challenge	Design solution
Data processing rigidity	Channel-independence, sample-wise normalization, temporal patching (Sec. 3.2)
Architectural constraints	GPT with causal attention, freeze-and-finetune strategy (Secs. 3.2–3.3)
Training and error propagation	Two-stage TeaF→SchS fine-tuning (Sec. 3.3)

Table 2: Universality Comparison of Methods

Method	Universality Scenarios			Single Model
	Stable/Unstable OCs	Unseen Faults	Heterogeneous System	
PINN [29]	×	×	×	✓
LSTM [5]	✓	×	×	×
PFNN [1]	✓	×	×	✓
FNO [30]	✓	×	×	✓
SVDKR [31]	✓	✓	×	×
DNR [8]	✓	✓	×	✓
TSA-LLM	✓	✓	✓	✓

2. Preliminary and Problem Formulation

2.1. Power System Model

Considering a power system containing n_b buses, n_g SGs, and n_l loads, the DAEs describing the system’s transient dynamics can be formulated as follows [1, 37]:

$$\begin{cases} \dot{\mathbf{x}}(t) = \mathbf{f}(\mathbf{x}(t), \mathbf{y}(t), \mathbf{u}(t), \mathcal{F}(t), t), \\ \mathbf{0} = \mathbf{g}(\mathbf{x}(t), \mathbf{y}(t), \mathbf{u}(t), \mathcal{F}(t), t), \end{cases} \quad (1)$$

where $\mathbf{x}(t) \in \mathbb{R}^{n_x}$ is the vector of dynamic state variables (e.g., rotor angles δ_i and angular speed ω_i of i -th SG), and $\mathbf{y}(t) \in \mathbb{R}^{n_y}$ is the vector of algebraic

variables (e.g., voltage magnitudes V_i of i -th bus). The vector $\mathbf{u}(t) \in \mathbb{R}^{n_u}$ represents control inputs, such as governor setpoints. The fault set $\mathcal{F}(t)$ denotes the system components experiencing faults. The nonlinear functions $\mathbf{f}(\cdot)$ and $\mathbf{g}(\cdot)$ describe the system dynamics and algebraic constraints, respectively.

2.2. Transformer Attention Mechanism

The transformer architecture has become the dominant backbone of modern large language models [32, 38, 39, 40] and has demonstrated remarkable success in sequence modeling, owing to its parallelizable computation and ability to capture long-range dependencies [41, 42]. At the core of this architecture is the self-attention mechanism. As illustrated in the bidirectional attention mechanism presented in Fig. 1(a), the process begins with an input sequence $\mathbf{X} = [\mathbf{x}(1), \mathbf{x}(2), \dots, \mathbf{x}(T)] \in \mathbb{R}^{T \times d}$, where T is the sequence length and d is the feature dimension, the bidirectional attention mechanism first transforms the input into three different representations: queries (\mathbf{Q}), keys (\mathbf{K}), and values (\mathbf{V}):

$$\mathbf{Q} = \mathbf{X}\mathbf{W}^Q, \quad \mathbf{K} = \mathbf{X}\mathbf{W}^K, \quad \mathbf{V} = \mathbf{X}\mathbf{W}^V, \quad (2)$$

where $\mathbf{W}^Q \in \mathbb{R}^{d \times d_k}$, $\mathbf{W}^K \in \mathbb{R}^{d \times d_k}$, and $\mathbf{W}^V \in \mathbb{R}^{d \times d_v}$ are learnable parameter matrices. The self-attention matrix is then computed as:

$$\text{Attention}(\mathbf{Q}, \mathbf{K}, \mathbf{V}) = \text{softmax} \left(\mathbf{Q}\mathbf{K}^T / \sqrt{d_k} \right) \mathbf{V}, \quad (3)$$

where $1/\sqrt{d_k}$ is a scaling factor to prevent vanishing gradients during training. In practice, Multi-Head Attention (MHA) is employed to enrich the model's expressive capability:

$$\text{MHA}(\mathbf{X}) = \text{Concat}(\text{head}_1, \text{head}_2, \dots, \text{head}_h) \mathbf{W}^O, \quad (4)$$

where $\text{head}_i = \text{Attention}(\mathbf{X}\mathbf{W}_i^Q, \mathbf{X}\mathbf{W}_i^K, \mathbf{X}\mathbf{W}_i^V)$. $\mathbf{W}_i^Q \in \mathbb{R}^{d \times d_k/h}$, $\mathbf{W}_i^K \in \mathbb{R}^{d \times d_k/h}$, $\mathbf{W}_i^V \in \mathbb{R}^{d \times d_v/h}$ are parameter matrices for the i -th attention head, $\mathbf{W}^O \in \mathbb{R}^{d_v \times d}$ is the output projection matrix, and h is the number of attention heads. By operating on the entire sequence, this bidirectional attention mechanism is well-suited for tasks like sequence translation and classification [41, 42].

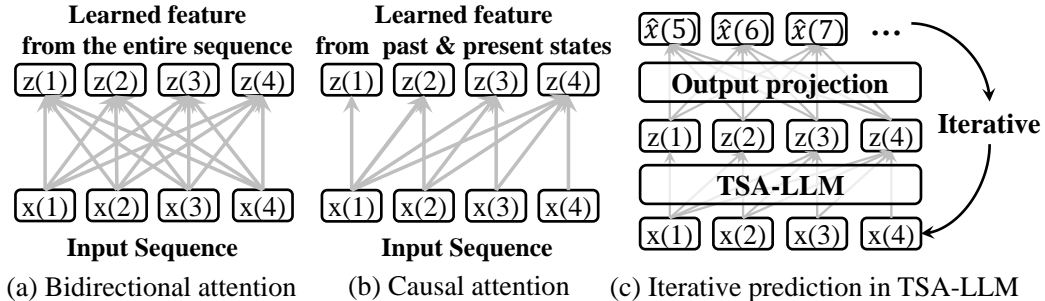


Fig. 1: Comparison of attention mechanisms and iterative prediction in TSA-LLM.

3. Methodology

This section details the proposed TSA-LLM, covering its data processing paradigm, the GPT-based architecture, and the two-stage fine-tuning scheme. Figure 2 illustrates the overall architecture and data workflow.

3.1. Data Processing

3.1.1. Channel Independence

The dynamic state variables of a power system are defined as the multivariate sequences:

$$\mathbf{x}(t) = [x_1(t), x_2(t), \dots, x_{n_x}(t)]^T, \quad (5)$$

where each $x_i(t) \in \mathbb{R}$ corresponds to a distinct state variable channel. Channel independence is formulated at the level of $\mathbf{x}(t)$: rather than treating $\mathbf{x}(t)$ as a fixed-dimensional vector sequence, we decompose it into a set of scalar sequences $\{x_i(t)\}_{i=1}^{n_x}$. Each channel is processed by an identical, shalblack pblackictor after applying the same segmentation and temporal-patch tokenization. This channel-wise shalblack modeling yields a dimension-agnostic input/output interface, and thus eliminates the need to reparameterize the model to match the system-specific value of n_x .

For clarity, we use the rotor angle as a concrete example and denote $\delta(t) = [\delta_1(t), \dots, \delta_{n_g}(t)]^T$, where n_g is the number of SGs (e.g., $n_g = 10$ for the IEEE 39-bus system and $n_g = 54$ for the IEEE 118-bus system). Across heterogeneous systems, n_g varies with the network configuration, and so does the dimension of $\delta(t)$. Channel independence addresses this mismatch by mapping $\delta(t) \in \mathbb{R}^{n_g}$ to $\{\delta_i(t)\}_{i=1}^{n_g}$ and applying the same shalblack pblackictor

to each channel. Consequently, TSA-LLM does not rely on any fixed system-level input/output dimension and can be directly reused across systems with different generator numbers without architecture blackefinition.

Moreover, TSA-LLM keeps the model interface trajectory-centric: the inputs are measublack/simulated post-fault trajectories without concatenating explicit topology/parameter tables such as Y -bus, line parameters, or generator parameters. In this setting, topology- and parameter-dependent coupling effects are learned from the response patterns embedded in the transient trajectories, which preserves a unified interface that is convenient to reuse across heterogeneous systems.

3.1.2. Segmentation and Sample-wise Normalization

Each univariate sequence $x_i \in \mathbb{R}^T$ is first partitioned into input-target samples via a sliding window of length $L_{\text{sam}} = L_{\text{seq}} + L_{\text{pblack}}$ with a unit stride. Each sample contains an input sequence of length L_{seq} and its corresponding pblackiction target of length L_{pblack} . The input portion, $x_{ij,\text{input}} \in \mathbb{R}^{L_{\text{seq}}}$, is then subjected to sample-wise normalization to ensure numerical stability, particularly for high-magnitude unstable trajectories:

$$x_{ij} = (x_{ij,\text{input}} - \mu_{ij})/\sigma_{ij} \in \mathbb{R}^{L_{\text{seq}}}, \quad (6)$$

where the mean μ_{ij} and standard deviation σ_{ij} are computed from $x_{ij,\text{input}}$ rather than the entire training set. This sample-wise normalization, as presented in Fig. 2(b), not only manages the extreme values of OOS SGs but also obviates the need for separate normalization statistics for stable/unstable SGs, a common practice in other methods [5]. Crucially, our approach eliminates the requirement for an online stability classification that may introduce both processing delays and the risk of error [31], thus guaranteeing a more robust and streamlined framework suitable for real-time application.

3.1.3. Temporal Patch

The final data processing step is temporal patch, designed to enhance both feature representation and modeling efficiency. Each normalized sample x_{ij} is partitioned into P overlapping patches of length L_p with a stride S , yielding a new, more compact representation $x_{ij}^P \in \mathbb{R}^{P \times L_p}$ as illustrated in Fig. 2(c). The number of patches P is given by:

$$P = \lfloor (L_{\text{seq}} - L_p)/S \rfloor + 1, \quad (7)$$

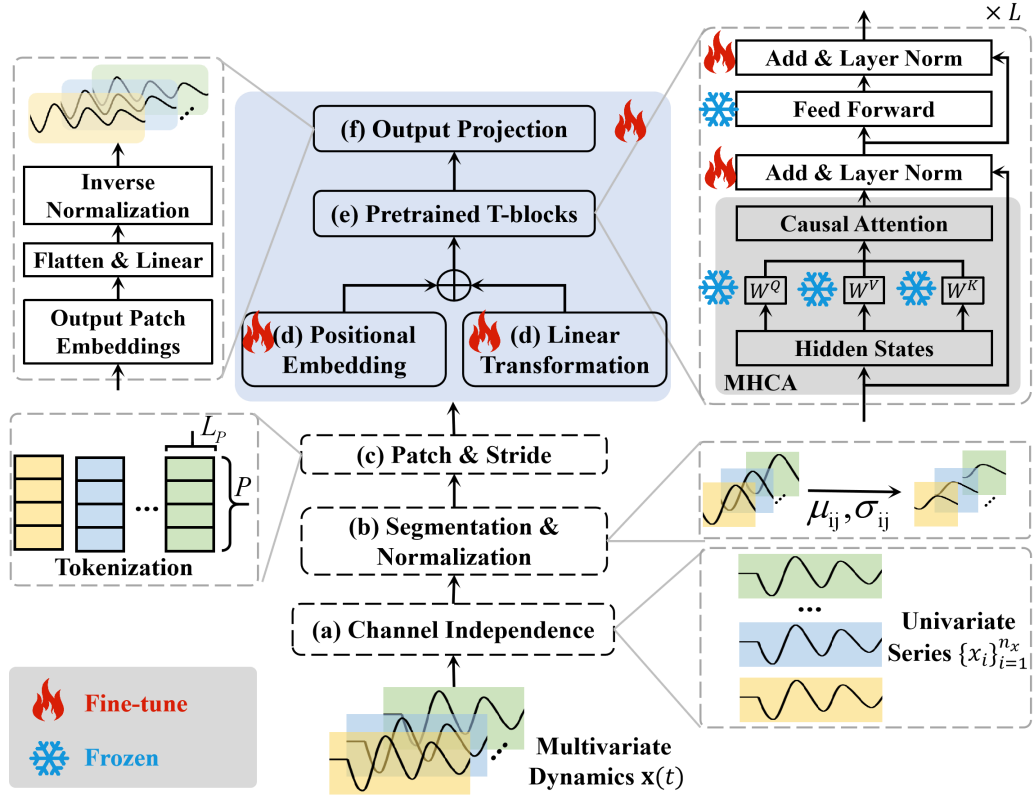


Fig. 2: Model structure and pipeline of TSA-LLM.

where $\lfloor \cdot \rfloor$ is the floor function. This patch-based tokenization enables the model to capture rich, local dynamic patterns (e.g., transient oscillations) that are more informative than isolated time points. Concurrently, by strategically blackcutting the input sequence length from L_{seq} to P , it is instrumental in mitigating the quadratic complexity ($\mathcal{O}(N^2)$) of the attention mechanism [41], thereby ensuring the computational tractability of long-sequence modeling.

3.2. Augmented GPT Architecture for TSA

Blackcutting long-horizon post-fault dynamics from a short observation window is intrinsically ill-posed, because multiple future trajectories may be consistent with the same limited history and small modeling errors can rapidly accumulate over long rollouts [1]. To align with the time-evolution nature of post-fault transients, we adopt an iterative autoregressive formulation: the model generates the future trajectory step-by-step, and each blackcut

is conditioned on the observed history and all previously generated states [8]. This yields a strictly causal factorization of the conditional distribution, which is mathematically consistent with the next-token generation principle in generative LLMs:

$$p(\hat{x}_{ij,\text{target}} \mid x_{ij,\text{input}}) = \prod_{t=L_{\text{scq}}+1}^{L_{\text{sam}}} p(x_{ij}(t) \mid x_{ij}(<t)). \quad (8)$$

Motivated by this alignment, we adopt a Generative Pre-trained Transformer (GPT) backbone [43] and adapt it for transient trajectory generation. In particular, GPT’s causal self-attention naturally enforces temporal causality and provides a strong sequence prior for robust long-horizon autoregressive rollout. The subsequent sections describe the resulting GPT-based architecture of TSA-LLM.

3.2.1. Input Embedding

The input embedding layer transforms the patch-structured samples $x_{ij}^P \in \mathbb{R}^{P \times L_p}$ into the initial hidden state \mathbf{z}_{ij}^0 . This process is defined as:

$$\mathbf{z}_{ij}^0 = x_{ij}^P \cdot \mathbf{W}^P + \mathbf{b}^P + \mathbf{E}_{\text{pos}} \in \mathbb{R}^{P \times d}. \quad (9)$$

In this formulation, each patch in x_{ij}^P is first mapped to an embedding of dimension d via a learnable linear projection with weight matrix $\mathbf{W}^P \in \mathbb{R}^{L_p \times d}$ and bias vector $\mathbf{b}^P \in \mathbb{R}^d$. Subsequently, a positional encoding matrix, $\mathbf{E}_{\text{pos}} \in \mathbb{R}^{P \times d}$, is added to this projection, which is learned dynamically during fine-tuning to provide the model with essential information about the absolute and relative positions of each patch. This final representation, \mathbf{z}_{ij}^0 , thus contains both the features of each patch and their sequential context, ready for processing by the transformer layers.

3.2.2. Transformer Block Architecture

The backbone of TSA-LLM is composed of a stack of L T-blocks adapted from the GPT model, as illustrated in Fig. 2(e). Each block performs a transformation that refines an input sequence \mathbf{z}^{l-1} into an output sequence \mathbf{z}^l :

$$\mathbf{z}^l = \text{Transformer-Block}(\mathbf{z}^{l-1}), \text{ for } l = 1, \dots, L. \quad (10)$$

This transformation is executed via two primary sub-layers—a multi-head causal self-attention mechanism (MHCA) and a position-wise feed-forward

network (FFN)—both embedded within a residual framework that utilizes skip connections and layer normalization.

The MHCA layer containing h parallel causal attention heads, endows the model with the ability to dynamically focus on relevant past information, as illustrated in Fig. 1(b). Within each head, \mathbf{z}_{ij}^0 is projected into queries (\mathbf{Q}), keys (\mathbf{K}), and values (\mathbf{V}) using (2) to compute causal attention scores:

$$\text{Cal-atten}(\mathbf{Q}, \mathbf{K}, \mathbf{V}) = \text{softmax} \left(\frac{\mathbf{Q}\mathbf{K}^T}{\sqrt{d_k}} + \mathcal{M}_{\text{causal}} \right) \mathbf{V}, \quad (11)$$

where the lower-triangular mask, $\mathcal{M}_{\text{causal}}$, is formulated as follows. Here, r and c denote the row and column indices (i.e., the query-token position and the key-token position) in the attention-score matrix.

$$\mathcal{M}_{\text{causal}}(r, c) = \begin{cases} 0 & \text{if } r \geq c, \\ -\infty & \text{otherwise.} \end{cases} \quad (12)$$

Pivotal to this operation is the causal mask, $\mathcal{M}_{\text{causal}}$, which nullifies the influence of future tokens by setting their corresponding attention scores to $-\infty$. This architectural constraint is what makes the model inherently suitable for iterative, generative tasks, as it forces the model to generate predictions based solely on available historical data, mimicking online dynamics prediction [34]. The outputs of the h heads are subsequently concatenated and linearly transformed by \mathbf{W}^O to yield the multi-head representation as shown in (13).

$$\text{MHCA}(\mathbf{z}_{ij}^0) = \text{Concat}(\text{Cal-atten}_1, \dots, \text{Cal-atten}_h) \mathbf{W}^O \quad (13)$$

The output of the multi-head attention sub-layer, after a residual connection and layer normalization, is then passed through a position-wise FNN, formulated as follows:

$$\begin{aligned} \mathbf{h}_{\text{att}} &= \text{LayerNorm}(\text{MHCA}(\mathbf{z}_{ij}^0) + \mathbf{z}_{ij}^0), \\ \mathbf{z}_{ij}^1 &= \text{LayerNorm}(\text{FFN}(\mathbf{h}_{\text{att}}) + \mathbf{h}_{\text{att}}), \end{aligned} \quad (14)$$

where the FNN module introduces nonlinearity through a two-layer fully connected network:

$$\text{FFN}(\mathbf{h}_{\text{att}}) = \text{GELU}(\mathbf{h}_{\text{att}} \cdot \mathbf{W}_1 + \mathbf{b}_1) \cdot \mathbf{W}_2 + \mathbf{b}_2. \quad (15)$$

In (15), $\mathbf{W}_1 \in \mathbb{R}^{d \times d_{\text{ff}}}$, $\mathbf{W}_2 \in \mathbb{R}^{d_{\text{ff}} \times d}$ are learnable parameters and d_{ff} is the hidden dimension. $\text{GELU}(\cdot)$ activation provides a smooth and nonlinear transformation, while the final projection \mathbf{W}_2 maps features back to the input dimensionality d , facilitating the composition of deep transformer architectures through block stacking.

3.2.3. Output Projection

The output layer transforms the final latent representation from the transformer, $\mathbf{z}_{ij}^L \in \mathbb{R}^{P \times d}$, into the pblackiction sequence, as illustrated in Fig. 2(f). The process begins by flattening the patch-level representations in a single vector $z_{ij}^{\text{flat}} = \text{Flatten}(z_{ij}^L) \in \mathbb{R}^{Pd}$ to consolidate all temporal features. This flattened vector is then mapped to the desiblack pblackiction horizon, via a learnable linear projection:

$$x_{ij}^{\text{pblack}} = z_{ij}^{\text{flat}} \cdot \mathbf{W}^{\text{out}} + \mathbf{b}^{\text{out}} \in \mathbb{R}^{L_{\text{pblack}}}, \quad (16)$$

where $\mathbf{W}^{\text{out}} \in \mathbb{R}^{Pd \times L_{\text{pblack}}}$ and $\mathbf{b}^{\text{out}} \in \mathbb{R}^{L_{\text{pblack}}}$ are the learnable weights and biases. To restore the pblackiction to its original physical scale, an inverse normalization operation is applied:

$$\hat{x}_{ij,\text{target}} = \sigma_{ij} \cdot x_{ij}^{\text{pblack}} + \mu_{ij}, \quad (17)$$

where the mean (μ_{ij}) and standard deviation (σ_{ij}) are the same values stoblack from the input sample’s normalization step (see (6)). The resulting vector, $\hat{x}_{ij,\text{target}} \in \mathbb{R}^{L_{\text{pblack}}}$, represents the final physical pblackiction for the target sequence of length L_{pblack} .

3.3. Two-Stage Fine-tune Strategy

3.3.1. Freeze-and-Finetune Strategy

To balance adaptation to the TSA task with the preservation of knowledge from pre-trained T-blocks, we propose a parameter-efficient fine-tuning strategy. In this approach, the core T-blocks are kept frozen, while only the parameters of task-specific components, namely the input embedding layer, the layer normalization, and the output projection head, are updated during fine-tuning as illustrated in Fig. 2. This strategy is designed to preserve the robust, generic feature extraction capabilities that the T-blocks acquire during pre-training. As detailed in Appendix A, the T-blocks are inherently optimized to find self- and cross-alignments within input sequences during the pre-training stage, making them powerful, modality-agnostic sequence feature

extractors. Freezing the T-blocks leverages this proven capability. The efficacy of this strategy is validated in our case study. The high feature stability and co-direction (detailed in Section 4.8) confirm that the generic features extracted by the pre-trained T-blocks are highly effective for power system dynamics sequences. The following sections detail the proposed two-stage fine-tuning approach, where TeaF trains on sequence segments with ground truth sequences as input, and SchS addresses trajectory-level learning with probabilistically mixed inputs of model pblackictions and ground truth.

Algorithm 1: Teacher Forcing Fine-Tuning

- 1: **Input:** TSA-LLM \mathbf{F} , Training set D_{train} , Epochs E_{TeaF} , Learning rate α , Integer K
 - 2: **Initialize:** Optimizer for \mathbf{F} with learning rate α
 - 3: **for** $k = 1, 2, \dots, E_{\text{TeaF}}$ **do**
 - 4: **for** each sample $(x_{ij,\text{input}}, x_{ij,\text{target}}) \in D_{\text{train}}$ **do**
 - 5: $\hat{x}_{ij,\text{target}} \leftarrow \mathbf{F}(x_{ij,\text{input}})$
 - 6: $\mathcal{L}_{\text{TeaF}} \leftarrow \text{MSE}(\hat{x}_{ij,\text{target}}, x_{ij,\text{target}})$
 - 7: Perform back-propagation on $\mathcal{L}_{\text{TeaF}}$ and update \mathbf{F}
 - 8: **end for**
 - 9: **end for**
 - 10: Initialize empty list L_{errors}
 - 11: **for** each trajectory $x_i \in D_{\text{train}}$ **do**
 - 12: $\hat{x}_i \leftarrow \text{IterativePblackict}(\mathbf{F}, x_i)$
 - 13: $e \leftarrow \text{MSE}(\hat{x}_i, x_i)$, Add (e, x_i) to L_{errors}
 - 14: **end for**
 - 15: Sort L_{errors} by error in descending order
 - 16: $D_{\text{hard}} \leftarrow$ top K trajectories from L_{errors}
 - 17: **Output:** Pre-trained model \mathbf{F} , Hard-case set D_{hard}
-

3.3.2. Teacher Forcing Stage

During the first TeaF stage, the proposed TSA-LLM, represented by $\mathbf{F}(\cdot)$, is conditioned on the ground-truth input segments, $x_{ij,\text{input}}$, to generate a pblackiction for the target sequence (denoted as $\hat{x}_{ij,\text{target}} = \mathbf{F}(x_{ij,\text{input}})$). The model parameters are optimized by minimizing the mean squablack error (MSE) loss, $\mathcal{L}_{\text{TeaF}}$, between the pblackicted output and the ground-truth

target:

$$\mathcal{L}_{\text{TeaF}} = \frac{1}{L_{\text{pblack}}} \sum_{t=1}^{L_{\text{pblack}}} (\hat{x}_{ij,\text{target}}(t) - x_{ij,\text{target}}(t))^2. \quad (18)$$

This TeaF stage, as presented in Algorithm 1, provides a robust model initialization that accelerates convergence in subsequent SchS phases while enabling the model to achieve high fidelity on less complex transient trajectories. It is noteworthy that for numerous existing approaches, their entire training process consists solely of this TeaF paradigm [8, 5, 34]. However, the iterative pblackiction process employed in online TSA application, where the TSA-LLM recursively conditions on its own outputs as illustrated in Fig. 1(c), presents a training-inference mismatch. The model, trained via TeaF on ground-truth data, suffers from this mismatch and is not equipped to handle its own pblackiction errors, leading to cumulative error propagation in complex unstable trajectories [44].

3.3.3. Schedule Sampling Phase

To mitigate the previously described training-inference mismatch, a scheduled sampling fine-tuning stage is proposed. Following a curriculum learning strategy [44], SchS focuses on the top- K error-prone trajectories, denoted by $x_i(t) \in D_{\text{hard}}$ for $t \in [1, T]$ identified within D_{train} , as identified in Algorithm 1. This top- K selection, rather than using the full set of trajectories, offers three key advantages: (i) it avoids gradient dilution, since the full set contains many “easy” trajectories where the model already performs well after TeaF, whose gradients would dominate and dilute the signal from hard cases that need improvement [45]; (ii) it blackuces computational cost, as SchS requires full iterative pblackiction over each trajectory and training on the full set would incur substantially higher per-epoch cost; and (iii) it allocates the limited SchS training budget to the trajectories that most impact online deployment, where cumulative error and training-inference mismatch are most severe. Critically, by emulating the iterative, self-conditioned pblackiction of online deployment, this process compels the model to develop robustness against its own error accumulation, thereby improving long-horizon iterative pblackiction in online TSA tasks.

During SchS stage, given an initial input sequence $x_{i,\text{input}} \in \mathbb{R}^{L_{\text{seq}}}$ spanning time steps $[1 : L_{\text{seq}}]$ from trajectory x_i , the model first generates a pblackiction

for the next time window $[L_{\text{seq}} + 1, L_{\text{seq}} + L_{\text{pblack}}]$:

$$\hat{\mathbf{x}}_{i,\text{target}} = \mathbf{F}(x_{i,\text{input}}) \in \mathbb{R}^{L_{\text{pblack}}}. \quad (19)$$

To generate the subsequent pblackiction, a new input sequence, $x_{i,\text{input}}^{\text{next}}$, is constructed by sliding the window forward. The core of the SchS strategy lies in how this new input is assembled. It consists of a known segment from the original ground-truth trajectory ($x_{i,\text{orig}}$) and a "mixed" segment ($x_{i,\text{mixed}}$), which is probabilistically sampled from either the ground-truth target ($x_{i,\text{target}}$) or the model's own previous pblackiction ($\hat{x}_{i,\text{target}}$):

$$x_{i,\text{mixed}} = \begin{cases} x_{i,\text{target}}, & \text{with probability } \varepsilon_k \\ \hat{x}_{i,\text{target}}, & \text{with probability } 1 - \varepsilon_k \end{cases} \quad (20)$$

where ε_k is the sampling rate for the current epoch k . The new input for the model is then a concatenation of these segments:

$$x_{i,\text{input}}^{\text{next}} = [x_{i,\text{orig}}, x_{i,\text{mixed}}]. \quad (21)$$

This probabilistic mixing is governed by a sampling rate ε_k that follows a linear decay schedule across training epochs. This gradually transitions the model from teacher forcing ($\varepsilon_k = 1$) to a fully iterative mode ($\varepsilon_k = 0$):

$$\varepsilon_k = \begin{cases} 1, & \text{if } k < E_{\text{start}} \\ 1 - \frac{k - E_{\text{start}}}{E_{\text{max}} - E_{\text{start}}}, & \text{otherwise} \end{cases} \quad (22)$$

where E_{start} is the epoch at which decay begins, and E_{max} is the maximum training epoch in SchS stage. The fine-tuning loss, $\mathcal{L}_{\text{SchS}}$, aggregates the MSE across the pblackicted trajectory sequence $\hat{x}_i(t)$:

$$\mathcal{L}_{\text{SchS}} = \frac{1}{(T - L_{\text{seq}})} \sum_{t=L_{\text{seq}}+1}^T (\hat{x}_i(t) - x_i(t))^2. \quad (23)$$

The complete SchS procedure is detailed in Algorithm 2.

Algorithm 2: Scheduled Sampling Fine-Tuning

- 1: **Input:** Pre-trained model \mathbf{F} , Hard-case set D_{hard} , Epochs E_{max} ,
Scheduled epoch E_{start} , Learning rate α
 - 2: **Initialize:** Optimizer for \mathbf{F} with learning rate α
 - 3: **for** $k = 1, 2, \dots, E_{\text{max}}$ **do**
 - 4: Calculate sampling probability ε_k using Eq. (22)
 - 5: **for** each trajectory $x_i \in D_{\text{hard}}$ **do**
 - 6: **Initialize:** Total loss $\mathcal{L}_{\text{SchS}} \leftarrow 0$
 - 7: $x_{i,\text{input}} \leftarrow x_i(1 : L_{\text{seq}})$
 - 8: **for** $j = 1, 2, \dots, \lfloor (T - L_{\text{seq}}) / L_{\text{pblack}} \rfloor$ **do**
 - 9: $\hat{x}_{i,\text{target}} \leftarrow \mathbf{F}(x_{i,\text{input}})$
 - 10: $\mathcal{L}_{\text{SchS}} \leftarrow \mathcal{L}_{\text{SchS}} + \text{MSE}(\hat{x}_{i,\text{target}}, x_{i,\text{target}})$
 - 11: $x_{i,\text{input}}^{\text{next}} \leftarrow$ Construct next input with $x_{i,\text{input}}$, $\hat{x}_{i,\text{target}}$,
 $x_{i,\text{target}}$, and ε_k based on (20) and (21)
 - 12: $x_{i,\text{input}} \leftarrow x_{i,\text{input}}^{\text{next}}$
 - 13: **end for**
 - 14: Perform back-propagation on $\mathcal{L}_{\text{SchS}}$
 - 15: Update model \mathbf{F} parameters
 - 16: **end for**
 - 17: **end for**
 - 18: **Output:** Final fine-tuned TSA-LLM
-

3.4. Online Application

While channel independence processes each of the n_x state variables separately in the offline fine-tuning stage, we mitigate potential computational overhead in online applications by treating the n_x channels as a unified mini-batch to exploit GPU parallelization and concurrent pblackict of all state variables. The online pblackiction begins with an initial multivariate observation from PMUs, denoted as $\mathbf{x}_{\text{input}}^{(0)} \in \mathbb{R}^{n_x \times L_{\text{seq}}}$. This multi-channel input is decomposed into n_x independent univariate patch sequences $\mathbf{x}_{\text{patch}}^{(0)} \in \mathbb{R}^{P \times L_P}$ as described in subsection 3.1, which are then stacked along the batch dimension via $\text{Batch}(\cdot)$, forming $\mathbf{x}_{\text{batch}}^{(0)} \in \mathbb{R}^{n_x \times P \times L_P}$. The TSA-LLM then pblackicts the target sequence of all state variables $\hat{\mathbf{x}}_{\text{target}}^{(0)} \in \mathbb{R}^{n_x \times L_{\text{pblack}} \times 1}$. Then, iterative pblackiction for each step j is performed sequentially as

follows:

$$j \in [1, \lfloor \frac{T-L_{\text{seq}}}{L_{\text{pblack}}} \rfloor] : \begin{cases} \mathbf{x}_{\text{input}}^{(j)} = \mathbf{x}_{\text{input}}^{(j-1)} \oplus \hat{\mathbf{x}}_{\text{target}}^{(j-1)}, \\ \mathbf{x}_{\text{patch}}^{(j)} = \text{Preprocess}(\mathbf{x}_{\text{input}}^{(j)}), \\ \mathbf{x}_{\text{batch}}^{(j)} = \text{Batch}(\mathbf{x}_{\text{patch}}^{(j)}), \\ \hat{\mathbf{x}}_{\text{target}}^{(j)} = \mathbf{F}(\mathbf{x}_{\text{batch}}^{(j)}), \end{cases} \quad (24)$$

where \oplus denotes the sliding window update mechanism, which discards the oldest input segment and appends the latest pblackiction, and $\text{Preprocess}(\cdot)$ follows the data processing pipeline in subsection 3.1. This fully iterative online pblackiction aligns with the SchS strategy where the sampling probability ϵ_k fixed at 0, forcing the model to rely entirely on its own generated trajectory.

3.5. Performance Indices Evaluation

To provide a comprehensive analysis, the model’s performance is evaluated on three distinct stability situations. The stable (S) situation comprises trajectories exclusively from stable OCs, while the unstable (U) situation contains only those from unstable OCs. A third, hybrid (H) situation is composed of a combination of both stable and unstable trajectories to assess overall generalization. The performance metrics (MAE , MSE) for each category $C \in \{S, U, H\}$ are formally defined by averaging the error over all trajectories in the corresponding stability situations:

$$\begin{aligned} MAE_C &= \sum_{x \in \mathcal{D}_C} \sum_{i=1}^{n_x} \sum_{t=L_{\text{seq}}+1}^T \frac{|\hat{x}_i(t) - x_i(t)|}{|D_C| \cdot n_x \cdot (T - L_{\text{seq}})}, \\ MSE_C &= \sum_{x \in \mathcal{D}_C} \sum_{i=1}^{n_x} \sum_{t=L_{\text{seq}}+1}^T \frac{(\hat{x}_i(t) - x_i(t))^2}{|D_C| \cdot n_x \cdot (T - L_{\text{seq}})}, \end{aligned} \quad (25)$$

where D_C is the test set for category C , $|D_C|$ is the number of trajectories within it, and $T_{\text{pblack}} = T - L_{\text{seq}}$ is the pblackiction length. The terms $\hat{x}_i(t)$ and $x_i(t)$ denote the pblackicted and ground-truth values, respectively, for the i -th dynamic trajectories at time t . This categorized analysis allows us to not only quantify but also explain the performance disparities observed in its handling of stable versus unstable system dynamics.

4. Case study

The proposed TSA-LLM framework is rigorously evaluated on the New England 39-bus system [8] and the modified Iceland 189-bus system [46]. On the New England 39-bus system, we assess the framework’s zero-shot generalization to mixed-stability OCs and unseen faults and conduct a representation analysis of its unstable OC handling mechanism. The Iceland 189-bus system is used to validate the model’s few-shot scalability on a more complex, heterogeneous grid. The evaluation is completed with analyses of training/inference costs, an ablation study of model components, and a final qualitative demonstration of the performance enhancements gained from using frozen T-blocks.

4.1. Data Generation and Model Settings

4.1.1. Test System and Simulation Settings

Two standard test systems were applied: the New England 39-bus system (10 SGs, 34 lines) and the modified Iceland 189-bus system (33 SGs, 206 lines). The latter was adapted for 20% RES penetration by replacing two SGs with wind units whose speeds were sampled from a Weibull distribution [47, 48]. Simulations include $N - 1$, $N - 2$, and $N - 3$ faults for the New England 39-bus system and $N - 1$ faults for the Iceland 189-bus system. For each contingency, simulations are conducted as follows: 1) All system loads were randomly varied between 70% and 130% of their nominal values; 2) An optimal power flow was solved using MATPOWER to establish the pre-fault OCs; 3) All SGs were represented by the fourth-order model; 4) Each contingency was simulated by applying the specified number of concurrent three-phase-to-ground faults to random lines at $t = 1.0$ s and cleared after a random duration of up to 0.3 s; 5) The post-fault dynamic response was simulated for 10 seconds with a 0.02 s time step by Power System Analysis Toolbox.

4.1.2. Dataset Organization

For fine-tuning and validation, a primary dataset of 9,000 trajectories (rotor angles and speeds) was generated from $N - 1$ contingencies on the 39-bus system, covering a mix of stable and unstable trajectories. This was partitioned into 8,000 training (D_{train}) and 1,000 validation (D_{val}) trajectories. Each trajectory was then segmented via a sliding window ($L_{\text{seq}} = 65$, $L_{\text{pblack}} = 1$) to yield approximately 1.8×10^7 training and 2×10^6 validation samples.

Additionally, trajectories from the 189-bus system were generated to evaluate cross-system few-shot adaptation on a more complex, heterogeneous grid. Model performance was evaluated against four distinct test sets, each designed to assess a specific aspect of universality. The details of these datasets are summarized in Table 3. The subsequent analysis primarily presents rotor angle pblackictions and results for other variables like rotor speeds are analogous and detailed in subsection 4.6. For the heterogeneous-system adaptation study on the 189-bus system, we generated a target-system corpus of 9,900 trajectories under $N - 1$ contingencies and randomly split it into $D_{\text{train}}^{189\text{bus}}$ (6,600 trajectories) and $D_{\text{test}}^{189\text{bus}}$ (3,300 trajectories). Unless otherwise stated, the *few-shot* setting uses 5% of $D_{\text{train}}^{189\text{bus}}$ (i.e., 330 trajectories) for adaptation and reports the results on $D_{\text{test}}^{189\text{bus}}$. The few-shot subset is sampled at the trajectory level (rather than at the sliding-window sample level) to avoid information leakage across overlapping windows, and the same segmentation pipeline is then applied to construct supervised input–target pairs. To further illustrate the data-efficiency trend of cross-system adaptation, we additionally report results under increasing target-data ratios on other heterogeneous benchmark systems (subsection 4.10).

Table 3: Test Sets Overview

Test Set	Tested Universality	Test Mode	System	Fault	Trajectories
D_{test}^{N-1}	Mixed OCs	Zero-shot	39-bus	$N - 1$	1000
D_{test}^{N-2}	Unseen faults	Zero-shot	39-bus	$N - 2$	1,000
D_{test}^{N-3}	Unseen faults	Zero-shot	39-bus	$N - 3$	1,000
$D_{\text{test}}^{189\text{bus}}$	Heterogeneous system	Few-shot	189-bus	$N - 1$	3,300

4.1.3. Baseline Selection Rationale

The selection of baseline methods for comparison is guided by three key principles: (1) representativeness of state-of-the-art TSA methods, (2) architectural diversity to isolate the contribution of key design choices, and (3) reproducibility and fair comparison.

First, we include the DNR framework [8] (143K parameters) and LSTM-based approach [5] (34K parameters) as they represent the current state-of-

the-art in TSA trajectory prediction. DNR is selected because it is the most recent unified framework that handles both stable and unstable OCs within a single model, making it the strongest existing baseline for universality evaluation. The LSTM baseline [5] is included as it represents the classical recurrent architecture widely adopted in TSA trajectory prediction, enabling us to assess the benefits of transformer-based architectures over traditional RNNs. Notably, LSTM has been the most frequently used baseline for comparison in recent TSA trajectory prediction studies [8, 31], further justifying its inclusion. Second, we include an Encoder-only Transformer (ENC) baseline (9.6M parameters) to isolate the contribution of causal attention mechanisms. The ENC baseline employs bidirectional attention, contrasting with our causal attention mechanism, thereby allowing us to demonstrate the importance of temporal causality in iterative prediction tasks.

Several methods referenced in Table 2 (PINN [29], PFNN [1], FNO [30], SVDKR [31]) are excluded from quantitative comparison due to fundamental methodological incompatibilities: (1) PINN lacks explicit design considerations for the three universality dimensions addressed in this work—namely, mixed stable/unstable operating conditions, generalization to unseen fault scenarios, and cross-system transferability—rendering it unsuitable for universality evaluation; (2) FNO operates in the frequency domain and necessitates distinct data preprocessing pipelines, introducing confounding factors that preclude equitable comparison with time-domain approaches; (3) SVDKR adopts a probabilistic prediction paradigm, which fundamentally differs from deterministic trajectory forecasting and impedes direct quantitative assessment against deterministic baselines. Furthermore, preliminary evaluation of PFNN [1] revealed performance characteristics comparable to the classical LSTM baseline under universal scenarios, thereby providing limited additional insight. Consequently, our comparative analysis focuses on LSTM, DNR, and ENC, which collectively encompass the requisite architectural diversity and constitute the most pertinent baselines for evaluating universality in TSA trajectory prediction.

4.1.4. Model Implementation Details

The proposed TSA-LLM, based on the GPT architecture (124M parameters, 12 layers, 12 heads, 768-dim embedding), was fine-tuned for up to 10 epochs using a two-stage TeaF and SchS scheme. Training utilized the Adam optimizer with a 1×10^{-4} initial learning rate managed by a cosine annealing scheduler and an early stopping criterion. To evaluate its per-

formance, TSA-LLM was benchmarked against three baseline models. The first two are the DNR framework from [8] and a standard LSTM network as presented in [5], for which we employed the hyperparameter settings as reported in their respective publications. The third baseline is an Encoder-only Transformer (ENC), constructed based on [41] to highlight performance differences arising from different attention mechanisms. This ENC model employs the bidirectional attention mechanism and is configured with 3 transformer layers, 6 bidirectional attention heads, and a 128-dim embedding. The parameter counts are 124M (total) and 858K (trainable, 0.69% of the total) for TSA-LLM, 34K for LSTM [5], 143K for DNR [8], and 9.6M for ENC. All baselines were implemented for multivariate dynamics prediction in PyTorch and trained on NVIDIA A100 GPU.

4.2. Evaluation on Mixed Stability OCs

4.2.1. Performance Comparison

This section evaluates the model’s robustness against mixed stable or unstable OCs on the D_{test}^{N-1} , which is collected in {S, U, H} situations as discussed in subsection 3.5. The quantitative results are summarized in Table 4, where bold and underlined values denote the best and second-best performance, respectively. As shown, TSA-LLM substantially outperforms all baseline models across nearly all metrics, with the performance gap being most pronounced in challenging unstable and hybrid cases. While traditional methods like DNR and LSTM struggle significantly in these scenarios with DNR’s MSE_U value even exceeding 100, TSA-LLM achieves remarkable error reductions. Specifically, TSA-LLM reduces MAE_U , MSE_U , MAE_H , and MSE_H by at least 84.49%, 97.27%, 83.49%, and 97.68%, respectively, compared to baselines. These quantitative findings are further corroborated by visualization of the rotor angle trajectories predicted by TSA-LLM in Fig. 3, which show a close tracking of the ground truth. For improved clarity, Fig. 4 further presents representative trajectory comparisons for SG 10 with predictions and ground truths plotted on the same axes. This significant disparity in performance can be attributed to fundamental architectural differences. Traditional RNN-based models (LSTM and DNR) suffer from vanishing gradient issue and exhibit constrained model capacity, which fundamentally limits their ability to capture complex nonlinear dynamics in unstable trajectory prediction. In contrast, the transformer architecture, utilized by both our proposed TSA-LLM and the ENC baseline, is far more effective at capturing long-range temporal dependencies, resulting in demonstrably superior

Table 4: New England 39-Bus System: Evaluation Results on Mixed Stability OCs

Model	MAE_S	MSE_S	MAE_U	MSE_U	MAE_H	MSE_H
LSTM	0.120	0.282	2.675	19.269	0.946	5.932
DNR	0.128	0.200	7.073	133.614	1.934	35.367
ENC	<u>0.059</u>	0.006	<u>0.557</u>	<u>0.703</u>	<u>0.284</u>	<u>0.360</u>
TSA-LLM	0.055	<u>0.007</u>	0.415	0.525	0.156	0.137

accuracy in these challenging scenarios.

4.2.2. Explaining Robust Pblackiction in Unstable Scenarios

To further investigate the source of TSA-LLM’s robustness, we conducted an interpretive analysis focused on its feature representations of OOS dynamics, which are critical in unstable scenarios. We selected a typical unstable case from the 39-bus system where SG δ_5 loses synchronism (Fig. 5(a)). Final-layer feature representations for the OOS SG (δ_5) and two stable SGs (δ_1, δ_{10}) were then extracted and projected into 2D space from both TSA-LLM and an identically trained channel-independent LSTM model for visualization with t-SNE [49]. The t-SNE visualizations reveal a stark contrast between the two architectures. For TSA-LLM (Fig. 5(b)), features from δ_5 form a distinct and clearly separable cluster, indicating effective learning of instability characteristics. However, the LSTM model exhibits substantial mixing of these representations (Fig. 5(c)). This demonstrates the inherent difficulty of RNN architectures in distinguishing the unique behavior of OOS generators, which correlates with their lower pblackiction accuracy and underscores the superior feature learning of the proposed attention-based architecture.

4.3. Zero-shot Generalizability on Unseen Faults

This section evaluates the model’s zero-shot generalizability to unseen, severe contingencies ($N - 2$ and $N - 3$) under mixed stability conditions. As detailed in Table 5 and Table 6, all baseline models exhibited a significant performance collapse when confronted with unseen faults. The MSE_H for the RNN-based LSTM and DNR models surged by factors of approximately 13 and 30, respectively, compared to their $N - 1$ performance. Even the transformer-based ENC model underperformed, with its MSE_U exceeding 1.5. In contrast, TSA-LLM demonstrated superior zero-shot generalization, with its error on unstable samples (MAE_U, MSE_U) remaining remarkably

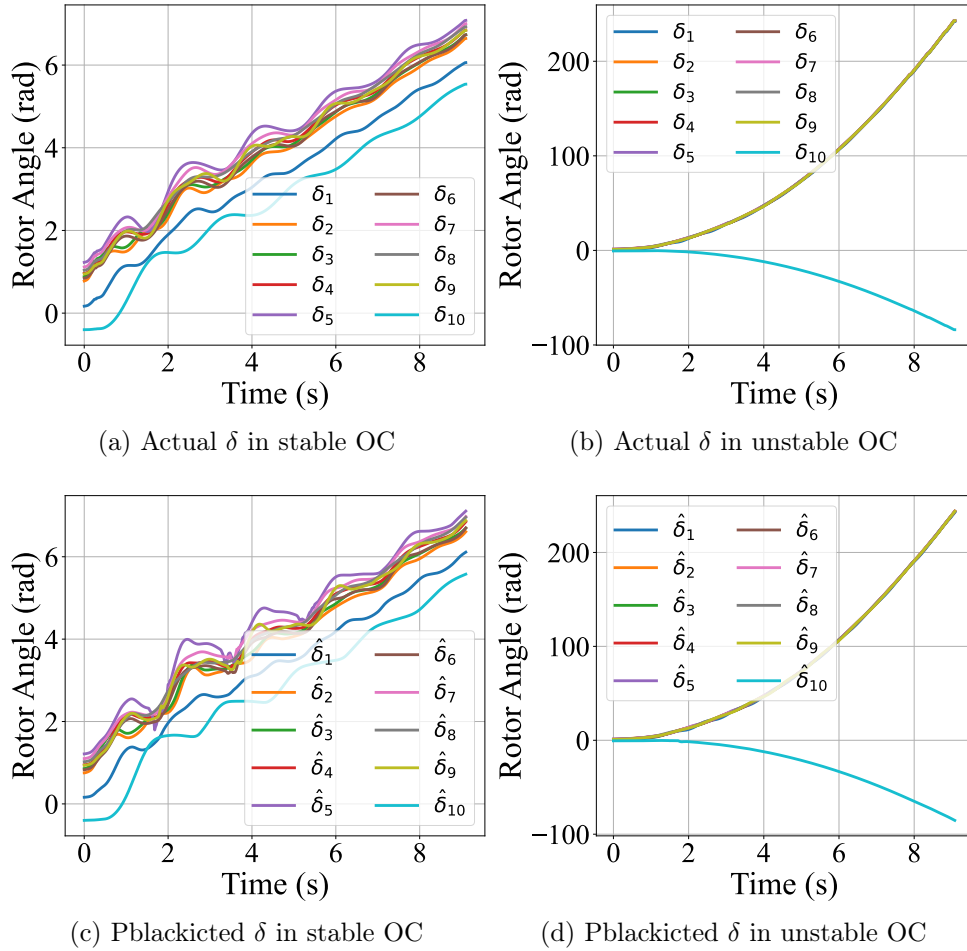


Fig. 3: New England 39-bus system: The evaluation of rotor angle under the stable and unstable OC. The pblackicted δ by TSA-LLM ((c) and (d)) demonstrates close alignment with ground truth ((a) and (b)).

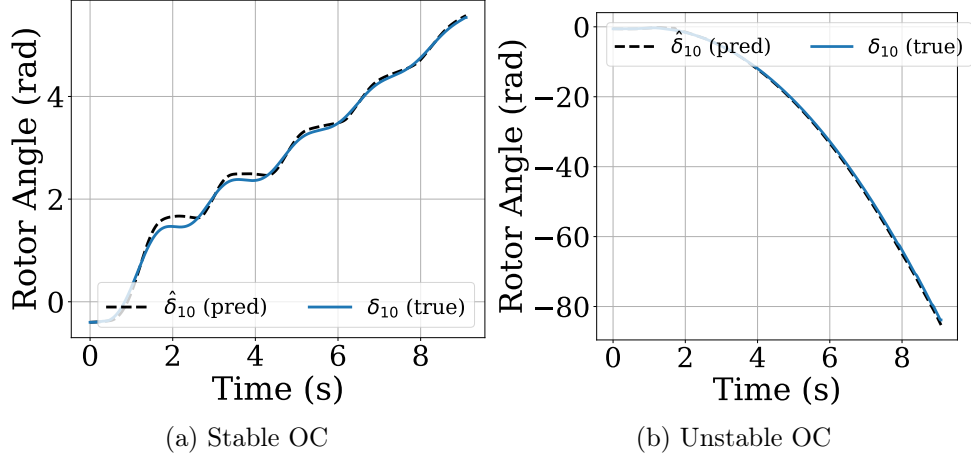


Fig. 4: Representative δ trajectory comparison for SG 10 (39-bus system). Predictions and ground truths are plotted on the same axes for improved clarity.

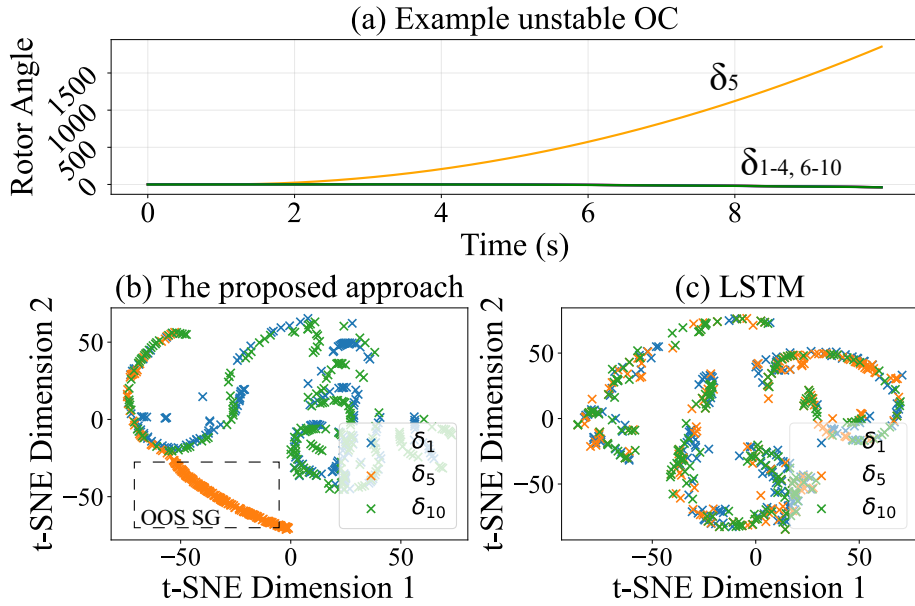


Fig. 5: The t-SNE visualization of stable/unstable sample feature maps for the proposed TSA-LLM and LSTM.

stable and increasing by less than 0.01 relative to the $N - 1$ scenario. This robustness provides a substantial advantage, with TSA-LLM blackucing MSE_H by nearly 71.05%–99.17% for $N - 2$ settings and 84.27%–99.78% for $N - 3$ settings relative to the baselines. These performance disparities are rooted in fundamental architectural and training differences. The failure of DNR, for instance, stems not only from the inherent modeling constraints of its RNN architecture but also from its lack of a mechanism to suppress error propagation, leading to severe error accumulation in complex and unstable scenarios. TSA-LLM incorporates a TeaF and SchS scheme specifically to build resilience to its own pblackictive errors, ensuring stable long-horizon forecasting. Furthermore, when compablack to the ENC baseline, TSA-LLM’s advantage is twofold. Its larger model scale provides greater expressive capacity, while its causal attention mechanism is better aligned with the nature of online TSA tasks than the ENC’s bidirectional attention, explaining its superior performance.

Table 5: New England 39-Bus System: Zero-shot Pblackiction Capacity Comparison under N-2 Setting

Model	MAE_S	MSE_S	MAE_U	MSE_U	MAE_H	MSE_H
LSTM	0.152	0.736	2.663	21.880	1.379	19.708
DNR	0.200	0.760	9.193	140.934	2.647	66.703
ENC	<u>0.083</u>	<u>0.010</u>	<u>0.793</u>	<u>1.593</u>	<u>0.781</u>	<u>0.563</u>
TSA-LLM	0.042	0.003	0.466	0.498	0.168	0.163

Table 6: New England 39-Bus System: Zero-shot Pblackiction Capacity Comparison under N-3 Setting

Model	MAE_S	MSE_S	MAE_U	MSE_U	MAE_H	MSE_H
LSTM	0.082	0.610	2.812	27.246	1.092	15.837
DNR	0.092	<u>0.020</u>	5.695	142.549	2.144	70.485
ENC	<u>0.031</u>	0.086	<u>0.864</u>	<u>1.567</u>	<u>0.671</u>	<u>0.981</u>
TSA-LLM	0.029	0.003	0.457	0.566	0.180	0.154

4.4. Scalability on heterogeneous system

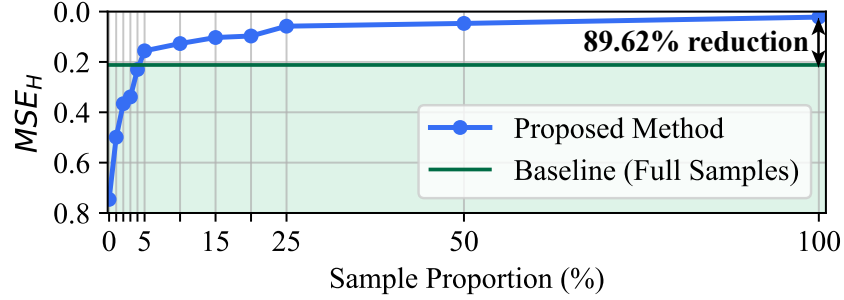
This section evaluates TSA-LLM’s ability to generalize and adapt to a heterogeneous power system with limited target-system data. The model’s

inherent cross-system potential was initially evaluated through a direct zero-shot test on the $D_{\text{test}}^{189\text{bus}}$ dataset, as its channel independence design permits direct application to systems of varying dimensions. Despite the significant topological and dynamic differences between the systems, TSA-LLM achieved an impressive MSE_H of approximately 0.752. This zero-shot performance is remarkably strong, even surpassing the in-distribution performance of baseline models like LSTM and DNR on their native New England 39-bus system, as shown in Table 4.

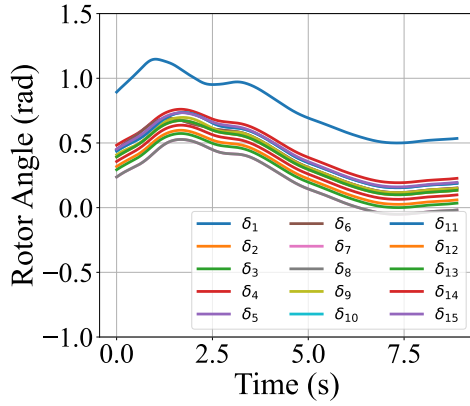
Furthermore, to assess the model’s few-shot learning capability, TSA-LLM pre-trained on the New England 39-bus system was further fine-tuned using varying proportions of $D_{\text{train}}^{189\text{bus}}$, employing the proposed TeaF and SchS schemes. Performance was subsequently evaluated on $D_{\text{test}}^{189\text{bus}}$. As shown in Fig. 6, the MSE_H of TSA-LLM rapidly decreases with increasing proportions of the Iceland 189-bus system fine-tuning data, and trends for other metrics are generally consistent. For a stringent comparison, the ENC model was trained on the full $D_{\text{train}}^{189\text{bus}}$ dataset to serve as an "expert" baseline for the target system. The results demonstrate that TSA-LLM achieves performance comparable to this fully-trained expert after fine-tuning on only 4%–5% of the available target-system data. This remarkable data efficiency is visually confirmed by the pblackicted trajectories from the TSA-LLM fine-tuned by 5% samples from $D_{\text{train}}^{189\text{bus}}$ in Fig. 6 and in Fig. 7, where pblackictions and ground truths for SG 2 are plotted on the same axes for improved clarity. Furthermore, when fine-tuned on the complete Iceland 189-bus system dataset, TSA-LLM blackuces the MSE_H by nearly 89.62% compablack to the expert ENC model, underscoring its superior architectural capacity. This cross-system performance introduces the potential to replace the costly, expert-intensive process of building custom-built models for large-scale systems by enabling an efficient methodology where a foundational model is trained on smaller systems and subsequently adapted with minimal target-system data. Beyond this immediate economic advantage, our findings reveal a clear path for true performance scalability. The model is designed to continually enhance its multi-system, multi-scenario proficiency by incorporating data from an ever-expanding corpus of power systems, paving the way for a single, continually evolving foundation TSA model.

4.5. Ablation Study

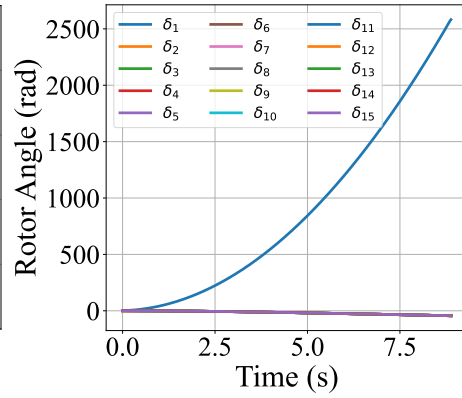
To assess the individual contributions of the dual-phase training strategy (TeaF and SchS) and the temporal patch, a series of ablation studies were



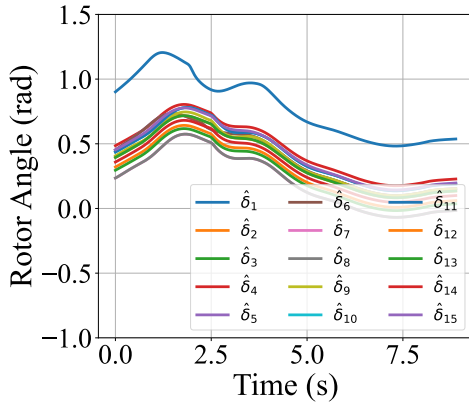
(a) Few-shot scalability



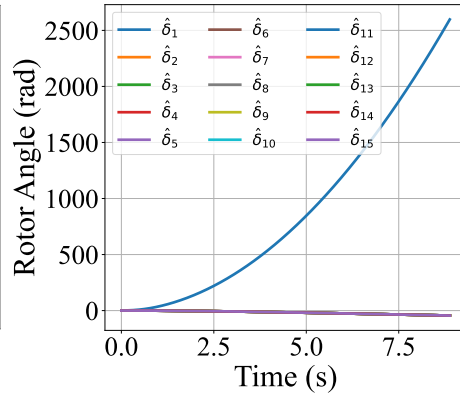
(b) Actual δ in stable OC



(c) Actual δ in unstable OC



(d) Pblackicted δ in stable OC



(e) Pblackicted δ in unstable OC

Fig. 6: Iceland 189-bus system: few shot scalability. To facilitate presentation, pblackiction results for a subset of 15 SGs are displayed.

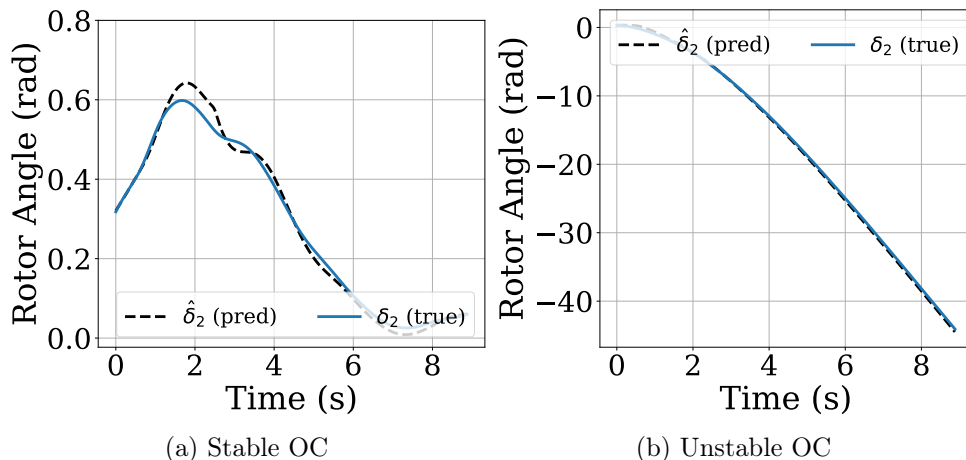


Fig. 7: Representative δ trajectory comparison for SG 2 (189-bus system). Pblackictions and ground truths are plotted on the same axes for improved clarity.

performed, with results summarized in Table 7. Model variants, denoted "w/o" for the exclusion of a component, were trained on the D_{train} and D_{val} . Their performance was subsequently evaluated across all test sets (D_{test}^{N-1} , D_{test}^{N-2} , D_{test}^{N-3} , and $D_{\text{test}}^{189\text{bus}}$), with a 5% fine-tuning step on $D_{\text{train}}^{189\text{bus}}$ applied specifically for the final cross-system test. The results confirm that all components are integral to the model's performance. The removal of TeaF and SchS, which form the dual-phase training strategy, led to the most significant performance degradation, with average error increases of nearly 68.76% and 41.16%, respectively, highlighting their importance in robustly modeling dynamics and suppressing cumulative errors. Lastly, removing the patch operation resulted in a nearly 21.26% performance decline, underscoring its importance in helping the attention mechanism model rich and informative local dynamic patterns.

4.6. Validation on Angular Speed

Recognizing the operational need for comprehensive state variable monitoring, this subsection evaluates the proposed model's pblackictive performance for rotor angular speed, with all pblackictions presented in per-unit (p.u.) values. As summarized in Table 8, the MSE_H results indicate that the proposed model demonstrates an even more substantial performance advantage in rotor speed pblackiction compblack to its rotor angle pblackiction

Table 7: Ablation Study Comparing the Performance of Full Proposed Model against Variants with Removed Components.

Model	D_{test}^{N-1}		D_{test}^{N-2}	
	MAE_H	MSE_H	MAE_H	MSE_H
w/o Teacher Forcing	0.194	0.296	0.241	0.329
w/o Schedule Sampling	0.189	0.178	0.192	0.258
w/o Patch	<u>0.161</u>	<u>0.145</u>	<u>0.192</u>	<u>0.230</u>
TSA-LLM	0.156	0.137	0.168	0.163
Model	D_{test}^{N-3}		$D_{\text{test}}^{189\text{bus}}(5\%)$	
	MAE_H	MSE_H	MAE_H	MSE_H
w/o Teacher Forcing	0.310	0.222	0.113	0.299
w/o Schedule Sampling	0.267	0.202	0.138	0.210
w/o Patch	<u>0.198</u>	<u>0.173</u>	<u>0.114</u>	<u>0.196</u>
TSA-LLM	0.180	0.154	0.072	0.156

capabilities. Across the four primary evaluation tasks, the proposed model achieves performance improvements of up to two orders of magnitude over baselines. For instance, when trained with the complete $D_{\text{train}}^{189\text{bus}}$, the proposed approach blackuced the MSE_H by nearly 95.95% relative to the leading baseline model (ENC) on $D_{\text{test}}^{189\text{bus}}$. Furthermore, in a few-shot learning scenario on this system, the proposed method matched the performance of the fully trained ENC model while utilizing only approximately 3% of the training data—a smaller proportion than requiblack for the rotor angle pblackiction task. These findings underscore the proposed method’s efficacy and versatility in pblackicting various critical state variables.

To further explore alternative data processing strategies, an additional experiment, TSA-LLM (Unit-wise), is conducted, as shown in the last row of Table 8. While the original TSA-LLM processes state variables independently to maximize cross-system adaptability, we investigate an alternative approach inspiblack by [31], where each synchronous generator (SG) is treated as an integrated unit. In this unit-wise formulation, the state trajectories of each SG (e.g., rotor angle δ and speed ω) are concatenated and jointly represented as multivariate time series, enabling the model to capture intra-unit correlations while maintaining inter-system generality. As shown in Table 8, the unit-wise variant achieves a 95.33% blackuction in MSE_H on the full $D_{\text{test}}^{189\text{bus}}$ and

matches the fully trained ENC baseline using only 3% of the training data. These results demonstrate that unit-wise temporal modeling provides a viable alternative for capturing variable dependencies while preserving cross-system flexibility.

Table 8: Angular Speed Pblackiction Performance Comparison by MSE_H

Model	D_{test}^{N-1}	D_{test}^{N-2}	D_{test}^{N-3}	$D_{\text{test}}^{189\text{bus}}(100\%)$
LSTM	0.0827	0.0904	0.1002	0.2036
DNR	0.0395	0.0457	0.0389	0.1235
ENC	0.0427	0.0478	0.0529	0.1136
TSA-LLM	0.0012	0.0008	0.0030	0.0056 (3%)
TSA-LLM (Unit-wise)	0.0010	0.00007	0.0034	0.0053 (3%)

4.7. Training and Inference Cost Comparison

This section analyzes the computational efficiency of the proposed TSA-LLM, comparing it against the ENC baseline and the traditional TDS on the large-scale 189-bus system. We assess efficiency using two key metrics: 1) the training cost per step, defined as a single forward and backward propagation pass on one batch, and 2) the inference time to pblackict the complete trajectories for a single operating condition (OC). The detailed results of this comparison are presented in Table 9.

4.7.1. Training Efficiency

The remarkable training efficiency of the large-scale TSA-LLM, which remains comparable to much smaller models, is almost entirely attributable to its parameter-efficient fine-tuning approach. The strategy of freezing the main T-blocks and training only 0.69% of the total parameters significantly blackuces the computational complexity associated with the most intensive phase of training, namely the backward pass and parameter update. This allows the model to be fine-tuned with exceptional speed, evidenced by a per-step training time on the large 189-bus system that is only negligibly slower (0.004s) than the compact ENC baseline.

4.7.2. Inference Speed

In the inference stage, TSA-LLM exhibits a significant speed advantage, proving faster than even the smaller ENC baseline on the 189-bus system. This high efficiency stems from three core design principles. First, the patch and stride operations strategically blackuce the input sequence length for the attention mechanism, which is instrumental in mitigating the quadratic computational complexity ($\mathcal{O}(N^2)$) inherent in long-sequence modeling. Second, the causal attention mechanism results in a sparse attention weight matrix where most elements are zero, thereby simplifying the computational process of aggregating patch representations. Most critically, the online application design reframes the problem by transforming all n_x system channels into the batch dimension. This enables the model to process the entire dynamic trajectory for a given operating condition simultaneously while fully leveraging the massive parallel processing capabilities of GPUs on large batches. Consequently, TSA-LLM not only outperforms the ENC model but also achieves an inference speedup of approximately 96.88% over traditional TDS. These results underscore the framework’s strong potential for efficient, real-time trajectory pblackiction.

It is worth clarifying that the reported 0.57 s corresponds to the end-to-end inference time under our specific hardware and implementation settings for pblackicting the complete post-fault trajectory over a 9 s horizon for one OC, and it is not a fundamental lower bound. In practical deployment, standard GPU inference optimizations (e.g., mixed precision/quantization and optimized runtime backends) can further blackuce latency. Moreover, for many unstable cases, system instability can often be identified from the early-stage response without requiring full-horizon pblackiction, implying that the effective response time for triggering emergency control can be substantially shorter than 0.57 s when a shorter screening horizon is adopted. Finally, our online application design batches all channels for concurrent pblackiction via GPU parallelization, so the inference time does not scale linearly with system size in the same way as time-domain simulation; as system scale increases and TDS becomes slower, the relative speed advantage of TSA-LLM is expected to be even more pronounced.

4.8. Generic Validation of Pre-trained Parameters

4.8.1. Performance Gain Attributable to Pre-training

Pre-trained T-blocks are a key factor behind the cross-scenario generalization of TSA-LLM. To quantify their contribution, we compablack TSA-LLM

Table 9: Training Parameters and Training/Inference Cost Comparison in the Modified Iceland 189-Bus System

Method	Trainable Params	Trainable Params Percentages	Training (s/step)	Inference (s/OC)
TDS	-	-	-	18.25
ENC	9.6M	100%	0.034	0.59
TSA-LLM	858K	0.69%	0.038	0.57

with a counterpart in which the T-block parameters were randomly initialized, using the same architecture and evaluation setting on D_{test}^{N-1} . As shown in Table 10, the randomly initialized model exhibits substantial performance degradation, while TSA-LLM achieves markedly lower errors, with about 86.23% and 99.41% blackuctions in MAE_H and MSE_H , respectively. These results indicate that pre-trained T-blocks within LLMs provide transferable sequence modeling priors for capturing transient power-system dynamics.

4.8.2. Explaining Performance Gains

After establishing the performance gap, we further investigated whether pre-trained T-blocks preserve the representational properties described in Appendix A. To align this analysis with the subsequent mechanism discussion, we used two indicators: *feature stability* and *feature co-directionality* (see Table 10).

Feature stability characterizes cross-layer consistency, i.e., whether the same patch remains similarly encoded as depth increases. We measure it by the mean cosine similarity between the representations of each patch in the last two Transformer layers. TSA-LLM attains 0.893, compared with 0.673 for the randomly initialized counterpart, indicating more stable feature propagation across layers.

Feature co-directionality characterizes intra-sequence alignment at a fixed layer. For each sequence, we compute pairwise cosine similarities among patch representations in the final layer and report the proportion of patch pairs with cosine similarity larger than 0.8. TSA-LLM reaches 71.44%, versus 46.78% without pre-training.

Overall, these results support the mechanism analysis in Appendix A and indicate that pre-trained T-blocks preserve transferable sequence representation properties for transient dynamics modeling. From a physical perspective, transient trajectories in power systems with synchronous generators are gov-

Table 10: Comparison of Model Performance with and without Pre-trained Parameters

Model	MAE_H	MSE_H
w/o pre-trained param	1.134	23.220
TSA-LLM	0.156	0.137
Model	Feature stability	Feature co-direction (>0.8)
w/o pre-trained param	0.673	46.78%
TSA-LLM	0.893	71.44%

erned by the same basic physics mechanisms, e.g., the swing equation coupled with network algebraic constraints. Therefore, after appropriate normalization, different systems often exhibit similar temporal evolution patterns despite differences in network scale and parameters. The stable temporal representations extracted by pre-trained T-blocks are effective in capturing these shablack patterns, which helps explain their strong performance in cross-scenario and cross-system generalization.

4.9. Backbone Replacement with Qwen3-0.6B

To further validate that the proposed framework is backbone agnostic, we instantiated TSA-LLM with an alternative pretrained decoder-only Transformer, Qwen3-0.6B. While both the original GPT backbone and Qwen3-0.6B adopt a decoder-only architecture, Qwen3-0.6B additionally uses a Mixture-of-Experts design. For a controlled comparison, we kept the data processing pipeline unchanged, including channel-independence, sample-wise normalization, and patching. We also used the same training protocol, including TeaF and SchS, and the same evaluation setup. In other words, we changed the backbone while holding all other components fixed.

Table 11 reports the resulting MSE_H scores. The Qwen3-0.6B (MoE) variant yields consistently lower errors than the original TSA-LLM across all four benchmarks, including D_{test}^{N-1} , D_{test}^{N-2} , D_{test}^{N-3} , and $D_{\text{test}}^{189\text{bus}}$ (5%).

These results lead to two observations. First, the TSA-LLM framework transfers naturally to other pretrained large-model backbones beyond GPT within the decoder-only family, which supports its architectural compatibility and portability. Second, increasing the effective model capacity via an MoE backbone appears to strengthen sequence representations and nonlinear dynamics modeling, improving long-horizon trajectory pblackiction in both

unseen-fault and cross-system settings. Overall, scaling the backbone provides a practical route to further enhance TSA universality and pblackiction accuracy.

Table 11: Estimated MSE_H comparison after backbone replacement with Qwen3-0.6B

Model	D_{test}^{N-1}	D_{test}^{N-2}	D_{test}^{N-3}	$D_{\text{test}}^{189\text{bus}}(5\%)$
TSA-LLM (GPT)	0.137	0.163	0.154	0.156
TSA-LLM (Qwen3-0.6B MoE)	0.126	0.149	0.141	0.142

4.10. Cross-System Scaling on the IEEE 68-bus System and the IEEE 118-bus System

To further strengthen the empirical justification of *universality* within the IEEE benchmark regime and to better illustrate the scaling trend beyond the IEEE-39/189 setting, we additionally evaluate TSA-LLM on two additional benchmark systems, namely the IEEE 68-bus system and the IEEE 118-bus system, under $N-1$ contingencies. The transient trajectories are generated following the same simulation pipeline described in Sec. 4.1 (*Data Generation and Model Settings*). This experiment is intended to provide additional benchmark evidence on cross-system scalability and data-efficiency, rather than to claim that IEEE-39 data alone can guarantee direct zero-shot generalization to real utility-scale grids with substantially higher heterogeneity and renewable penetration. Specifically, we generate 14,400 trajectories for the IEEE 68-bus system (16 SGs) and 17,100 trajectories for the IEEE 118-bus system (19 SGs), corresponding to 900 operating conditions (OCs) in total, and split each dataset into $D_{\text{train}}^{\text{target}}$ and $D_{\text{test}}^{\text{target}}$ with a 2:1 ratio (9,600/4,800 for the IEEE 68-bus system and 11,400/5,700 for the IEEE 118-bus system). In particular, the test set comprises 300 OCs, and the OCs are generated with a stable/unstable proportion of 7:3.

In addition to trajectory-pblackiction errors, we further report stability-relevant classification metrics derived from the pblackicted trajectories. Specifically, we define a transient stability index (TSI) based on the maximum rotor-angle separation with respect to the center-of-inertia (COI) [1, 50]. For an OC k , let $\delta_{i,k}(t)$ denote the rotor angle of generator i , and define

$$\Delta\delta_k(t) = \max_i |\delta_{i,k}(t) - \delta_{\text{COI},k}(t)|, \quad (26)$$

$$\text{TSI}_k = \max_{t \in [t_0, T]} \Delta\delta_k(t), \quad (27)$$

where $[t_0, T]$ is the post-fault simulation horizon. Given a pblackefined stability threshold δ_{th} (set to π), the ground-truth stability label is

$$y_k = \mathbb{I}(\text{TSl}_k > \delta_{\text{th}}) \in \{0, 1\}, \quad (28)$$

where $y_k = 1$ indicates an unstable (loss-of-synchronism) OC and $y_k = 0$ indicates a stable OC. The pblackicted label \hat{y}_k is obtained by applying the same rule to the pblackicted trajectories. We then report the classification accuracy (Acc) and the recall of the unstable class (Recall-U) as

$$\text{Acc} = \frac{1}{N} \sum_{k=1}^N \mathbb{I}(\hat{y}_k = y_k), \quad (29)$$

$$\text{Recall-U} = \frac{\sum_{k=1}^N \mathbb{I}(\hat{y}_k = 1) \mathbb{I}(y_k = 1)}{\sum_{k=1}^N \mathbb{I}(y_k = 1)}, \quad (30)$$

where N is the number of OCs in the test set.

We consider three transfer settings: (i) *zero-shot* evaluation, where the model is fine-tuned only on the IEEE 39-bus system and directly tested on the target system; (ii) *few-shot* adaptation on the target system with limited data ratios (10% and 20%); and (iii) *full-data* fine-tuning on the target system. For comparison, we also report the performance of the strongest baseline, ENC, trained with the full target-system data as an expert model.

Table 12 summarizes the results. On the IEEE 68-bus system, the zero-shot transfer from the IEEE 39-bus system attains an MSE_H of 0.620, and few-shot fine-tuning with only 10% target data already outperforms the full-data ENC expert (0.122 vs. 0.135). With 20% target data, the error is further blackuced to 0.106, and full-data fine-tuning reaches 0.082. A similar trend is observed on the IEEE 118-bus system, where MSE_H decreases from 0.710 (zero-shot) to 0.136 with 10% target data, surpassing the ENC expert trained on the full target data (0.149), and further improves to 0.113 (20%) and 0.089 (full-data). Notably, the conventional RNN baselines (LSTM and DNR) exhibit orders-of-magnitude larger trajectory errors and markedly lower unstable-recall, indicating their limited robustness in mixed stable/unstable post-fault settings.

For a supplementary comparison on the shablack task of transient stability classification, we further include the Potential Energy Boundary Surface (PEBS) method as a representative classical direct-method baseline [14]. PEBS is an energy-function-based method that approximates the post-fault

stability boundary by locating the first local maximum of the potential energy along the fault-on trajectory, thereby avoiding explicit UEP computation and retaining attractive screening efficiency for large contingency sets. Since PEBS outputs only stability decisions rather than pblackicted trajectories, MSE_H is not applicable. As shown in Table 12, PEBS attains Acc/Recall-U of 75.0%/76.7% on the IEEE 68-bus system and 77.7%/67.8% on the IEEE 118-bus system. Its unstable-class recall remains higher than those of the conventional RNN baselines, showing that PEBS can still capture a meaningful portion of critical unstable cases. However, its relatively modest overall accuracy suggests a conservative decision tendency, i.e., improved unstable-case coverage is achieved at the cost of more false alarms on stable OCs. By contrast, TSA-LLM consistently delivers both higher Acc and higher Recall-U, indicating a more balanced and reliable stability discrimination capability on these benchmark systems, while simultaneously providing full trajectory-level pblackiction and cross-system transfer capability.

Overall, these benchmark results indicate that TSA-LLM can be efficiently adapted to other benchmark systems with limited target-system data, while maintaining a clear improvement trend as the fine-tuning data increases. Extending the same framework to real utility-scale systems will require expanding the training corpus to cover larger-scale and renewable-rich dynamics, which we identify as future work.

Table 12: Cross-system scaling evaluation on the IEEE 68-bus system and the IEEE 118-bus system under $N-1$ contingencies.

Target system	Method/Setting	MSE_H	Acc (%)	Recall-U (%)
IEEE 68-bus	TSA-LLM (Zero-shot)	0.620	80.0	70.0
	TSA-LLM (Few-shot, 10%)	0.122	95.0	95.6
	TSA-LLM (Few-shot, 20%)	0.106	96.0	96.7
	TSA-LLM (Full-data)	0.082	97.0	97.8
	ENC (Full-data)	0.135	94.7	91.1
	LSTM (Full-data)	12.876	89.0	55.6
	DNR (Full-data)	9.516	90.3	60.0
	PEBS	-	75.0	76.7
IEEE 118-bus	TSA-LLM (Zero-shot)	0.710	78.0	68.9
	TSA-LLM (Few-shot, 10%)	0.136	94.3	94.4
	TSA-LLM (Few-shot, 20%)	0.113	95.3	96.7
	TSA-LLM (Full-data)	0.089	96.3	97.8
	ENC (Full-data)	0.149	94.0	90.0
	LSTM (Full-data)	15.083	88.0	51.1
	DNR (Full-data)	11.809	89.3	55.6
	PEBS	-	77.7	67.8

5. Conclusion

This paper introduces TSA-LLM, a universal framework that leverages a pre-trained LLM to achieve robust generalization across diverse OCs, unseen faults, and heterogeneous systems with a single architecture. This framework comprises a novel data processing pipeline featuring channel-independence, sample-wise normalization, and temporal patching to handle mixed-stability and long sequences from heterogeneous systems. Moreover, a parameter-efficient, freeze-and-finetune strategy for the augmented GPT architecture is designed to preserve generic sequence feature extraction from pre-trained T-blocks while allowing for TSA task adaptation. Furthermore, a two-stage finetuning scheme that combines TeaF with SchS is devised to mitigate cumulative pblackiction errors and ensuring long-horizon reliability. Case studies on two benchmark systems demonstrate that the proposed approach exhibits exceptional universality, low training and inference costs, and a considerable

degree of interpretability, establishing it as a promising foundation for real-time TSA.

5.1. Scope and Limitations

The proposed framework is validated on several standard IEEE test systems with different scales and operating characteristics. Regarding *system size*, TSA-LLM has demonstrated transferability across multiple benchmark systems. Extending it to utility-scale grids will mainly depend on systematic simulations on larger and more heterogeneous systems to construct representative training and evaluation datasets. Regarding the *diversity of operating conditions*, the present experiments include randomized load variations and wind-induced stochasticity. Broader coverage will require additional renewable scenarios and more general non-optimal pre-fault states generated beyond OPF-centblack settings. Regarding *disturbance types*, the current validation covers variation in fault location and contingency severity, but mainly under three-phase short-circuit faults. Extending the framework to a broader disturbance space will require incorporating additional symmetrical and asymmetrical faults, such as single line-to-ground and line-to-line faults. Regarding *model assumptions*, TSA-LLM follows a measurement-driven setting in which topology and parameter effects are learned implicitly from post-fault trajectories instead of being encoded explicitly. Relaxing this assumption will require introducing more explicit structural priors into the modeling framework.

5.2. Future Work

As future work, embedding specialized power system mechanism knowledge into the model structure or training objective (e.g., by adding physics informed regularization such as DAE/swing consistency residual losses) remains a promising direction worthy of further exploration, which may further enhance the framework’s interpretability and generalization under data-scarce or out-of-distribution scenarios. In addition, augmenting the input embedding with a topology-aware encoder (e.g., graph neural networks) to fuse explicit structural representations with sequence tokens is another promising extension. Identifying the optimal model scale for characterizing power system dynamics remains an open question and warrants further investigation.

Appendix A. Generic Feature Extraction of T-Blocks

The decision to freeze the T-blocks in GPT is grounded in their optimization during pre-training, which shapes them into generic sequence feature extractors. The self-attention input and mapping are first defined, followed by the gradient upper-bound result.

For a given channel index i and sample index j , we follow the notation in the main text and denote the input to the T-block as the embedded token matrix \mathbf{z}_{ij}^0 defined in (9). To simplify the analysis below, we rewrite it as

$$\mathbf{X} = \mathbf{z}_{ij}^0 = (x_1, \dots, x_P)^\top \in \mathbb{R}^{P \times d}, \quad (\text{A.1})$$

where P is the number of temporal patch tokens and, by a slight abuse of notation for notational simplicity, $x_m \in \mathbb{R}^d$ denotes the embedding of the m -th patch token (i.e., the m -th row of \mathbf{z}_{ij}^0). Define the self-attention mapping as

$$f(\mathbf{X}) = \text{softmax}(\mathbf{X}A\mathbf{X}^\top) \mathbf{X}, \quad (\text{A.2})$$

where $A = \mathbf{W}^Q(\mathbf{W}^K)^\top \in \mathbb{R}^{d \times d}$. Let $\mathbf{P} = \text{softmax}(\mathbf{X}A\mathbf{X}^\top)$ with entries

$$p_{m,n} = \frac{\exp(x_m^\top A x_n)}{\sum_{k=1}^P \exp(x_m^\top A x_k)}. \quad (\text{A.3})$$

Based on the gradient analysis of self-attention in [49, 51], the following bound holds.

Lemma A.1. Let $G = \left[\frac{\partial f(\mathbf{X})}{\partial x_m} \right]_{m=1}^P$ denote the Jacobian of $f(\mathbf{X})$ with respect to \mathbf{X} . Then,

$$\begin{aligned} |G|_2 \leq & |A|_2 \sum_m \left(p_{m,m} + \frac{1}{2} \right) \underbrace{\left| x_m - \sum_n p_{m,n} x_n \right|^2}_{\text{Self-alignment}} \\ & + |A|_2 \sum_{m \neq n} p_{m,n} \underbrace{\left| x_n - \sum_k p_{m,k} x_k \right|^2}_{\text{Cross-alignment}} + \frac{|A|_2}{2} \sum_m |x_m|^2. \end{aligned} \quad (\text{A.4})$$

Equation (A.4) provides a direct objective-level explanation for the effect of pre-training. During large-scale pre-training, parameter updates in self-attention tend to blackuce the gradient magnitude $|G|_2$; thus, optimization implicitly pushes down the right-hand side of (A.4). This induces two structublack alignment effects.

- First, the **Self-alignment** term $|x_m - \sum_n p_{m,n}x_n|^2$ shrinks the distance between each token representation x_m and its attention-weighted context $\bar{x}_m = \sum_n p_{m,n}x_n$, which improves feature consistency after repeated T-block transformations.
- Second, the **Cross-alignment** term $|x_n - \sum_k p_{m,k}x_k|^2$ is weighted by $p_{m,n}$. Therefore, token pairs with larger attention weights are more strongly constrained to align with the same contextual center $\sum_k p_{m,k}x_k$, yielding co-directional representations for strongly correlated tokens.

Together, these alignment dynamics tend to project token representations onto a compact and consistent principal subspace. Since this mechanism operates on ordered token sequences without restricting the form of X , it is independent of semantic modality and can be regarded as modality-agnostic. For power system transient prediction, such structured representation is particularly beneficial, as transient dynamics are typically dominated by a limited number of principal oscillatory modes. The alignment-induced projection concentrates trajectory information onto these dominant directions while suppressing redundant components, thereby stabilizing long-range dependency modeling and mitigating error accumulation during iterative forecasting. This optimization-induced generic feature extraction behavior explains why freezing the pre-trained T-block parameters remains effective for TSA tasks.

References

- [1] C. Shen, K. Zuo, M. Sun, Physics-following neural network for online dynamic security assessment, *IEEE Transactions on Power Systems* (2025).
- [2] R. Segurado, G. Krajačić, N. Duić, L. Alves, Increasing the penetration of renewable energy resources in s. vicente, cape verde, *Applied energy* 88 (2) (2011) 466–472.
- [3] N. Hatziargyriou, J. Milanovic, C. Rahmann, V. Ajjarapu, C. Canizares, I. Erlich, D. Hill, I. Hiskens, I. Kamwa, B. Pal, et al., Definition and classification of power system stability—revisited & extended, *IEEE Transactions on Power Systems* 36 (4) (2020) 3271–3281.

- [4] Z. Shi, W. Yao, L. Zeng, J. Wen, J. Fang, X. Ai, J. Wen, Convolutional neural network-based power system transient stability assessment and instability mode prediction, *Applied Energy* 263 (2020) 114586.
- [5] X. Ye, A. Radovanovic, J. V. Milanovic, The use of machine learning for prediction of post-fault rotor angle trajectories, *IEEE Transactions on Power Systems* 39 (5) (2024) 6496–6507.
- [6] Y. Zhao, M. Liu, C. Wang, Z. Wang, D. Chong, J. Yan, Exergy analysis of the regulating measures of operational flexibility in supercritical coal-fired power plants during transient processes, *Applied Energy* 253 (2019) 113487.
- [7] X. Zhan, S. Han, N. Rong, Y. Cao, A hybrid transfer learning method for transient stability prediction considering sample imbalance, *Applied Energy* 333 (2023) 120573.
- [8] T. Zhao, M. Yue, J. Wang, Structure-informed graph learning of networked dependencies for online prediction of power system transient dynamics, *IEEE Transactions on Power Systems* 37 (6) (2022) 4885–4895.
- [9] Z. Qiu, C. Duan, W. Yao, P. Zeng, L. Jiang, Adaptive lyapunov function method for power system transient stability analysis, *IEEE Transactions on Power Systems* 38 (4) (2022) 3331–3344.
- [10] Y. Xue, T. Van Cutsem, M. Ribbens-Pavella, Extended equal area criterion justifications, generalizations, applications, *IEEE Transactions on Power Systems* 4 (1) (1989) 44–52.
- [11] P. Kundur, et al., Power system stability, *Power system stability and control* 10 (1) (2007) 7–1.
- [12] H.-D. Chang, C.-C. Chu, G. Cauley, Direct stability analysis of electric power systems using energy functions: theory, applications, and perspective, *Proceedings of the IEEE* 83 (11) (1995) 1497–1529.
- [13] B. Berggren, G. Andersson, On the nature of unstable equilibrium points in power systems, *IEEE transactions on power systems* 8 (2) (2002) 738–745.

- [14] H.-D. Chiang, F. F. Wu, P. P. Varaiya, Foundations of the potential energy boundary surface method for power system transient stability analysis, *IEEE Transactions on Circuits and Systems* 35 (6) (1988) 712–728. doi:10.1109/31.1808.
- [15] Q. Zong, W. Yao, H. Zhou, H. Zhao, J. Wen, S. Cheng, Transient stability assessment of large-scale power system using predictive maximal lyapunov exponent approach, *IEEE Transactions on Power Systems* 39 (3) (2023) 5163–5176.
- [16] J. L. Willems, J. C. Willems, The application of lyapunov methods to the computation of transient stability regions for multimachine power systems, *IEEE Transactions on Power Apparatus and Systems* (5) (2007) 795–801.
- [17] S. K. Azman, Y. J. Isbeih, M. S. El Moursi, K. Elbassioni, A unified online deep learning prediction model for small signal and transient stability, *IEEE transactions on power systems* 35 (6) (2020) 4585–4598.
- [18] Q. Zhou, J. Davidson, A. Fouad, Application of artificial neural networks in power system security and vulnerability assessment, *IEEE Transactions on Power Systems* 9 (1) (1994) 525–532.
- [19] F. R. Gomez, A. D. Rajapakse, U. D. Annakkage, I. T. Fernando, Support vector machine-based algorithm for post-fault transient stability status prediction using synchronized measurements, *IEEE Transactions on Power systems* 26 (3) (2010) 1474–1483.
- [20] K. Sun, S. Likhate, V. Vittal, V. S. Kolluri, S. Mandal, An online dynamic security assessment scheme using phasor measurements and decision trees, *IEEE Transactions on Power Systems* 22 (4) (2007) 1935–1943. doi:10.1109/TPWRS.2007.908476.
- [21] Q. Chen, N. Lin, S. Bu, H. Wang, B. Zhang, Interpretable time-adaptive transient stability assessment based on dual-stage attention mechanism, *IEEE Transactions on Power Systems* 38 (3) (2022) 2776–2790.
- [22] C. Ren, Y. Xu, R. Zhang, An interpretable deep learning method for power system transient stability assessment via tree regularization, *IEEE Transactions on Power Systems* 37 (5) (2021) 3359–3369.

- [23] L. Zhu, W. Wen, J. Li, Y. Hu, Integrated data-driven power system transient stability monitoring and enhancement, *IEEE Transactions on Power Systems* 39 (1) (2023) 1797–1809.
- [24] H.-Y. Su, C.-C. Lai, Online transient stability margin estimation using improved deep learning ensemble model, *IEEE Transactions on Power Systems* 39 (6) (2023) 7421–7424.
- [25] L. Zhu, D. J. Hill, C. Lu, Hierarchical deep learning machine for power system online transient stability prediction, *IEEE Transactions on Power Systems* 35 (3) (2019) 2399–2411.
- [26] L. Zhu, D. J. Hill, Networked time series shapelet learning for power system transient stability assessment, *IEEE Transactions on Power Systems* 37 (1) (2021) 416–428.
- [27] W. Zou, D. Froning, Y. Shi, W. Lehnert, A least-squares support vector machine method for modeling transient voltage in polymer electrolyte fuel cells, *Applied energy* 271 (2020) 115092.
- [28] Y. Li, M. Zhang, C. Chen, A deep-learning intelligent system incorporating data augmentation for short-term voltage stability assessment of power systems, *Applied Energy* 308 (2022) 118347.
- [29] G. S. Misyris, A. Venzke, S. Chatzivasileiadis, Physics-informed neural networks for power systems, in: 2020 IEEE power & energy society general meeting (PESGM), IEEE, 2020, pp. 1–5.
- [30] W. Cui, W. Yang, B. Zhang, A frequency domain approach to predict power system transients, *IEEE Transactions on Power Systems* 39 (1) (2023) 465–477.
- [31] B. Tan, J. Zhao, Bayesian post-fault power system dynamic trajectory prediction, *IEEE Transactions on Power Systems* (2025).
- [32] J. Achiam, S. Adler, S. Agarwal, L. Ahmad, I. Akkaya, F. L. Aleman, D. Almeida, J. Altenschmidt, S. Altman, S. Anadkat, et al., Gpt-4 technical report, arXiv preprint arXiv:2303.08774 (2023).
- [33] S. Tu, Y. Zhang, J. Zhang, Z. Fu, Y. Zhang, Y. Yang, Powerpm: Foundation model for power systems, *Advances in Neural Information Processing Systems* 37 (2024) 115233–115260.

- [34] Y. Liu, H. Zhang, C. Li, X. Huang, J. Wang, M. Long, Timer: generative pre-trained transformers are large time series models, in: Proceedings of the 41st International Conference on Machine Learning, 2024, pp. 32369–32399.
- [35] C. Fan, J. Wang, W. Gang, S. Li, Assessment of deep recurrent neural network-based strategies for short-term building energy predictions, *Applied energy* 236 (2019) 700–710.
- [36] S. Karimi, S. Kwon, Optimization-driven uncertainty forecasting: Application to day-ahead commitment with renewable energy resources, *Applied Energy* 326 (2022) 119929.
- [37] S. Wen, H. Lan, Y.-Y. Hong, D. C. Yu, L. Zhang, P. Cheng, Allocation of ess by interval optimization method considering impact of ship swinging on hybrid pv/diesel ship power system, *Applied Energy* 175 (2016) 158–167.
- [38] A. Liu, B. Feng, B. Xue, B. Wang, B. Wu, C. Lu, C. Zhao, C. Deng, C. Zhang, C. Ruan, et al., Deepseek-v3 technical report, arXiv preprint arXiv:2412.19437 (2024).
- [39] C. Shen, Z. Guo, X. Wan, Z. Yang, Y. Zhang, W. Huang, J. Song, Z. Zhang, M. Sun, Proopf: Benchmarking and improving llms for professional-grade power systems optimization modeling, arXiv preprint arXiv:2602.03070 (2026).
- [40] C. Shen, Z. Guo, K. Zuo, W. Huang, M. Sun, Llm-dmd: Large language model-based power system dynamic model discovery, arXiv preprint arXiv:2601.05632 (2026).
- [41] A. Vaswani, N. Shazeer, N. Parmar, J. Uszkoreit, L. Jones, A. N. Gomez, Ł. Kaiser, I. Polosukhin, Attention is all you need, *Advances in neural information processing systems* 30 (2017).
- [42] M. Gao, S. Zhou, W. Gu, Z. Wu, H. Liu, A. Zhou, X. Wang, Mmgpt4lf: Leveraging an optimized pre-trained gpt-2 model with multi-modal cross-attention for load forecasting, *Applied Energy* 392 (2025) 125965.

- [43] A. Radford, J. Wu, R. Child, D. Luan, D. Amodei, I. Sutskever, et al., Language models are unsupervised multitask learners, *OpenAI blog* 1 (8) (2019) 9.
- [44] A. M. Lamb, A. G. ALIAS PARTH GOYAL, Y. Zhang, S. Zhang, A. C. Courville, Y. Bengio, Professor forcing: A new algorithm for training recurrent networks, *Advances in neural information processing systems* 29 (2016).
- [45] Q. Yu, Z. Zhang, R. Zhu, Y. Yuan, X. Zuo, Y. Yue, W. Dai, T. Fan, G. Liu, L. Liu, X. Liu, H. Lin, Z. Lin, B. Ma, G. Sheng, Y. Tong, C. Zhang, M. Zhang, W. Zhang, H. Zhu, J. Zhu, J. Chen, J. Chen, C. Wang, H. Yu, Y. Song, X. Wei, H. Zhou, J. Liu, W.-Y. Ma, Y.-Q. Zhang, L. Yan, M. Qiao, Y. Wu, M. Wang, Dapo: An open-source llm reinforcement learning system at scale (2025). *arXiv:2503.14476*.
URL <https://arxiv.org/abs/2503.14476>
- [46] H. Cai, H. Ma, D. J. Hill, A data-based learning and control method for long-term voltage stability, *IEEE Transactions on Power Systems* 35 (4) (2020) 3203–3212.
- [47] G. Lu, S. Bu, Advanced probabilistic transient stability assessment for operational planning: A physics-informed graphical learning approach, *IEEE Transactions on Power Systems* (2024).
- [48] Z. Shu, Q. Li, P. Chan, Investigation of offshore wind energy potential in hong kong based on weibull distribution function, *Applied Energy* 156 (2015) 362–373.
- [49] T. Zhou, P. Niu, L. Sun, R. Jin, et al., One fits all: Power general time series analysis by pretrained lm, *Advances in neural information processing systems* 36 (2023) 43322–43355.
- [50] C. Shen, K. Zuo, M. Sun, Physics-augmented auxiliary learning for power system transient stability assessment, *IEEE Transactions on Industrial Informatics* (2025).
- [51] H. Kim, G. Papamakarios, A. Mnih, The lipschitz constant of self-attention, in: *International Conference on Machine Learning*, PMLR, 2021, pp. 5562–5571.